Chapter 3

Experimental procedure

The versatility and possibility of low-cost large-scale application of chemical solution deposition (CSD) are among the main reasons for the choice of this methodology for the preparation of the samples presented in this work.

In this chapter we describe the thermal treatment of single-crystals substrates prior to deposition and, then, the experimental procedure followed for the preparation of nanostructured templates and $YBa_2Cu_3O_{7-x}$ (YBCO) thin films. Crystallographic structure of oxides used is also reported, except for the case of YBCO which has already been revised in the introductory chapter.

3.1 Substrates and surface treatment

There used to be a general tendency to consider substrates as a passive component in the growth of structures, with minimal repercussion on the final system. However, substrates act as the first template for epitaxial growth and, consequently, they are a key component to grow high quality structures with excellent properties. Therefore, extended efforts are deployed in last decades to study substrates' surfaces and to improve surface quality and smoothness [158]. Furthermore, new and interesting functionalities are arising due to the particularities of interfaces, where substrate's surface might play a crucial role [159-162]. Hence, it is highly important to select the substrate in agreement with the characteristics and goals of the system.

Some global issues to consider regarding substrate selection include chemical compatibility with the structure to be deposited on top, thermal expansion matching or surface cleanliness. For epitaxial growth, which requires the growth of a controlled crystallographic orientation in relation to substrate, lattice mismatch between structures is an important factor to take into account too (see also section 1.2.2). Moreover, coincidence of lattice sites improves the chance to achieve epitaxial growth. These are atomic positions which match up in either site of the interface; thus, it is preferable that atoms in these positions show close atomic sizes and valences. Obviously, surface and structural quality are also crucial requirements for the

substrate. Hence, it is highly demanding to have a good knowledge and control over substrates, and particularly, over its surface.

3.1.1 Treatment of substrate surface

Treatment of substrate's surface consists of processing the as-received substrates to ensure smooth impurity-free single-terminated surfaces. Through these treatments, surface substrate rearranges, either by diffusion or desorption of atoms, till it achieves the surface structure energetically more favourable. For vicinal (001) surfaces, the equilibrium structure exhibits atomically flat terraces separated by steps of height (n + ½)a, where a is the lattice parameter and n=1/2, 1, 3/2, 2…. Presence of steps is due to the miscut angle θ. There is always a misalignment from the (001) plane in the cut of the single-crystal, typically θ~0.1-0.2^{o}. As a result of this miscut, when (001)-surfaces rearrange show a stair-like morphology as schematized in Fig. 3-1.

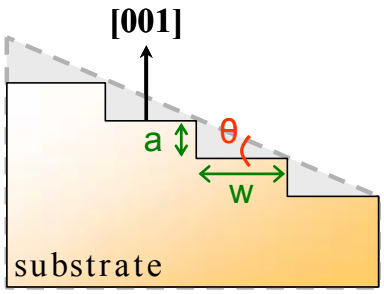

Fig. 3-1: Schematic representation of step's formation in (001)-surfaces as consequence of miscut angle θ. For a better visualization, θ has been extremely exaggerated.

There exists a large variety of processes in the literature to clean and prepare atomically flat surfaces, especially for the case of widely used $SrTiO_3$ (STO) substrates. Strategies range from ion bombardment cleaning [163] to chemical etching with NH_4F-HF solution of controlled pH [164].

All substrates used in this work were treated as follows to ensure clean atomically flat surfaces [165]. First, as-received substrates were subjected to ultrasonic agitation in acetone for 5 min and, then, in methanol for 5 min more. The role of ultrasonic agitation is to remove impurities from the surface, whereas stoichiometry is maintained. Second, substrates were heat treated to induce surface reorganization and to remove possible carbon-containing impurities still remaining on the surface. Substrates' annealing was carried out in quartz tube oven in constant oxygen flow of 0.5 l/min, which was regulated by a mass flow. They were heated at 900^{o}C/h till 900^{o}C; they remained 5 hours at this temperature and then they were cooled down to room temperature at 600^{o}C/h. The corresponding thermal profile is sketched in Fig. 3-2. To avoid possible external impurities, the quartz tube was cleaned prior to each treatment and substrates were covered with a clean crucible during annealing. On the other hand, to prevent

from problems related to aging or dirtying of the surfaces, treated substrates were used within a period of 15 days after annealing.

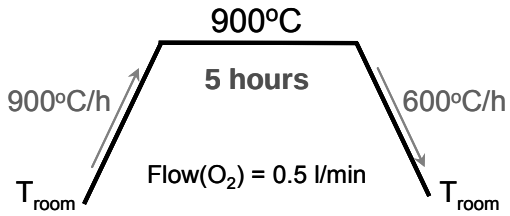

Fig. 3-2: Profile of the heat treatment used for the surface-conditioning of single-crystal substrates. Prior to deposition, all substrates were submitted to this thermal treatment.

The heating process described above was reported in literature for the case of STO substrates [165]; but we also applied it successfully to other phases like $LaAlO_3$ (LAO) as it is illustrated later. The commercial 5x5 mm^2 and 0.5 mm thick (001) single-crystal substrates used were from *Cristec*.

3.1.2 Perovskite-structure

The perovskite-type structure exhibited by many oxides can be summarized by the general chemical formula ABO_3, where A and B are cations. The ideal cubic perovskite unit-cell consists of type-B atoms located at cube corner sites (0,0,0), a type-A atom at the body centre positions (½, ½, ½) and oxygen atoms at mid-edge sites (i.e. (½, 0, 0)), as outlined in Fig. 3-3a. Viewed along <001> direction, the ABO_3 crystal consists of alternating stacks of A-O and B-O planes (Fig. 3-3b). This layered structured is important since it determines the termination of the single-crystal when cut orthogonally to one of its main axis.

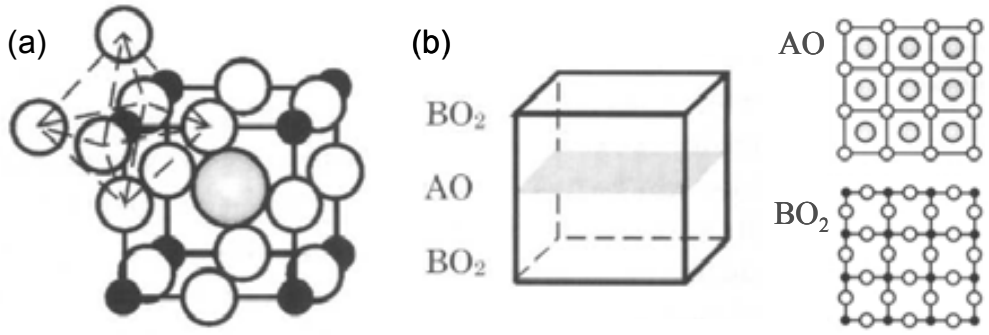

Fig. 3-3: Perovskite-type ABO_3 crystal structure. Schematic view of its unit-cell using the solid spheres model (a) and represented as alternating stacks of AO and BO_2 planes (b).

3.1.3 $SrTiO_3$ (STO) single-crystal substrates

Interest in STO surfaces is extensively spread specially because these substrates are very suitable for the epitaxial growth of oxide thin films in applications in many fields such as

high temperature superconductors (HTS), ferroelectricity or ionic conductivity [159, 166, 167]. STO is also a candidate to crystalline gate dielectric in silicon-based devices [168].

The crystal structure of STO is of perovskite-type ABO_3 with lattice parameter 3.905 Å. Its unit-cell (outlined in Fig. 3-4) is based on titanium atoms at the corner sites, and a strontium atom at the body centre site. Titanium atoms are surrounded by six oxygen atoms constituting an octahedron, i.e. oxygen atoms are at the middle of edge sites unit-cell. For STO, the two possible (001) bulk terminations are SrO surface and TiO_2 surface, both with neutral electric charge. Thus, depending on annealing conditions, (001)STO surface may exhibit SrO-termination, TiO_2-termination or a combination of both.

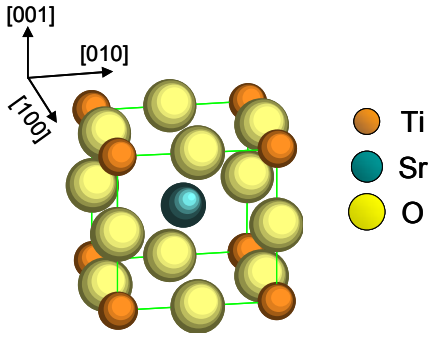

Fig. 3-4: Solid sphere model with ionic radius reduced by half (for a better visualization) showing the perovskite-type unit-cell of STO.

Fig. 3-5 shows a typical topographic image of an as-received (001)STO substrate; this substrate has a roughness rms~0.16 nm.

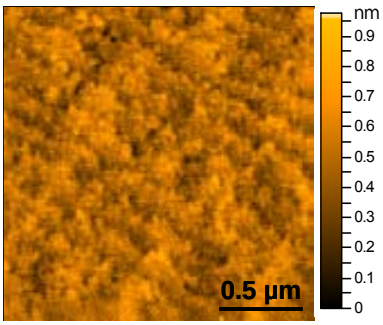

Fig. 3-5: Topographic AFM image of an as-received single-crystal (001)STO substrate.

Fig. 3-6 exhibits the typical surface of a (001)STO single-crystal substrate after being submitted to the described annealing treatment. Treated STO surfaces exhibit atomically flat terraces separated by one unit-cell high steps (Fig. 3-6d), indicative of a single-terminated surface. Accordingly to literature, the thermal process followed usually leads to the development of Sr-O terminated surfaces [165]. The particular termination achieved in our substrates was not investigated, given that the purpose of thermal treatments does not go further from obtaining clean atomically flat surfaces as similar as possible from one substrate to another

one. Nevertheless, it has been reported that flat terraces with curved edges, like the ones observed in Fig. 3-6a, correspond to Sr-O layers [169].

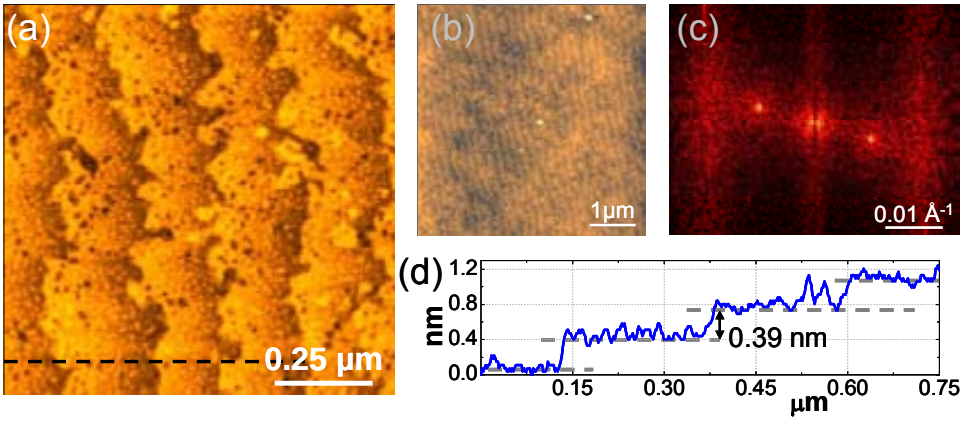

Fig. 3-6: Atomically flat surface separated by one unit-cell steps of a (001)STO single-crystal substrate after heat treatment described in section 3.1.1: 1x1 μm^2 (a) and 5x5 μm^2 (b) topographic AFM images; 2D-FFT of the 5x5 μm^2 AFM image (c), and profile showing step-like morphology of the surface (d).

Typically, terraces of our heat-treated STO surfaces are (140±60) nm width. These dimensions were determined from the periodicity indicated by 2D Fast Fourier Transform (FFT) (i.e., Fig. 3-6c) applied to 5x5 μm^2 AFM images (like the one in Fig. 3-6b). The separation between spots in the FFT image ($2\pi/v$) corresponds to the distance between the periodic events present in the analyzed image. Image size of 5x5 μm^2 was used since it exhibits enough and well-resolved steps so that to be confident of the value found. These terraces' width correspond to substrates with a miscut angle respect (001) plane of $\theta=(0.16\pm0.11)^o$.

3.1.4 $LaAlO_3$ (LAO) single-crystal substrates

Despite being less commonly used than STO, LAO single-crystals substrates are also very suitable, for example, for the epitaxial growth of HTS [170, 171] or other perovskite-based materials [172, 173].

At high temperature, LAO exhibits a perovskite-type (A=La, B=Al) simple cubic structure; and at T_c~500°C it experiences a second-order phase transition to the distorted perovskite rhombohedral structure typical of low temperatures, with lattice parameter a=b=c=5.355 Å and angles $\alpha=\beta=\gamma=60.1^o$ [174-177]. Therefore, it is generally treated as a pseudocubic perovskite structure with a=b=c=3.788 Å and angles $\alpha=\beta=\gamma=90.066^o$ (Fig. 3-7). As consequence of this transition, a twin domain structure develops to relieve strain when LAO is cooled below the critical temperature T_c. Particularly, LAO twins are (100) and (110) [178, 179].

The two possible terminations for (001)LAO surfaces are Al-O_2 and La-O layers, with negative (AlO_2^{2-}) and positive (LaO^{1+}) electrical charge, respectively. It has been observed that

(001)LAO surface termination is usually temperature dependent. Generally, at temperatures below 150°C, surfaces are Al-O terminated, whereas for T>250°C an exclusive La-O layer has been observed [180].

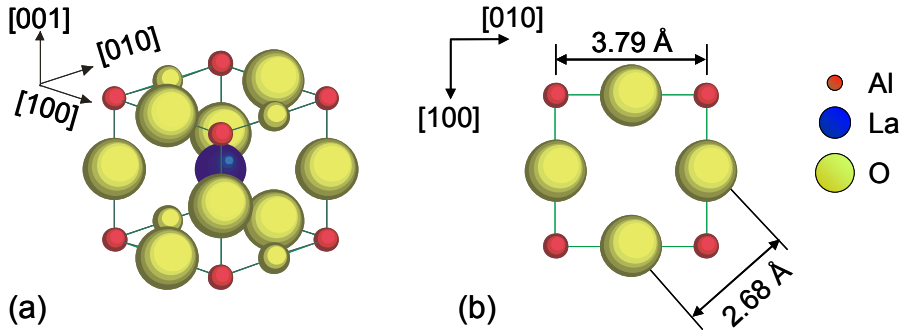

Fig. 3-7: Solid spheres model of the unit-cell of the perovskite LAO (a) and planar-view of the plane (001)-AlO_2. The ionic radius is reduced by 40% for better visualization.

AFM studies prove that (001)LAO surfaces with one unit-cell high steps are also obtained when substrates are submitted to thermal treatment described in section 3.1.1. An example is displayed in Fig. 3-8.

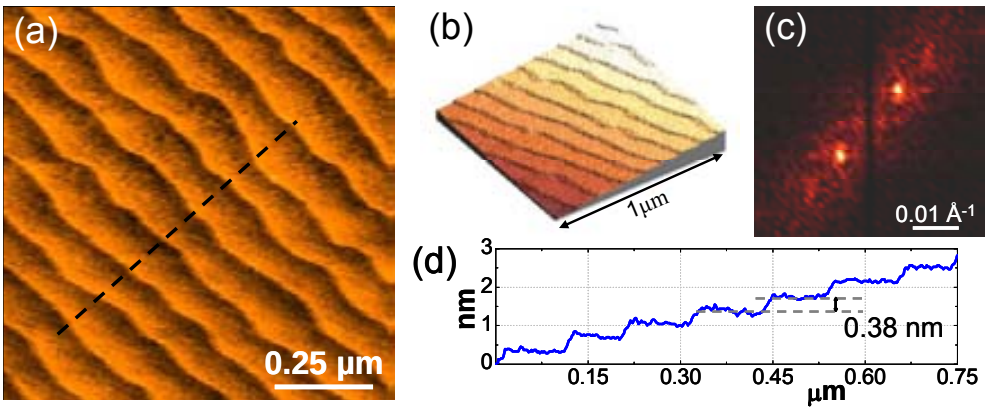

Fig. 3-8: (001)LAO surface after heat treatment described in section 3.1.1: 2D (a) and 3D (b) 1x1 μm^2 AFM topographic images; corresponding 2D-FFT (c) and profile (d) showing the morphology of periodic atomically-flat terraces separated by one unit-cell high steps.

For this particular example (Fig. 3-8), terraces are ~107 nm width. However, this width is not constant all over the LAO substrate surface since steps' orientation and terraces' width might change at each twin boundary, as observed in Fig. 3-9a and corresponding 2D-FFT in Fig. 3-9b. For example, in this case, steps at the upper side of the twin boundary are separated ~143 nm, whereas at the other side terraces' width is just ~75 nm; sizes which correspond to an "equivalent" miscut angle of ~0.15° and ~0.28°, respectively. This feature is due to the miscut and polishing of the substrate and later heat and cool trough the critical temperature T_c. Fig. 3-9c illustrates the sequence of processes that lead to such situation [175].

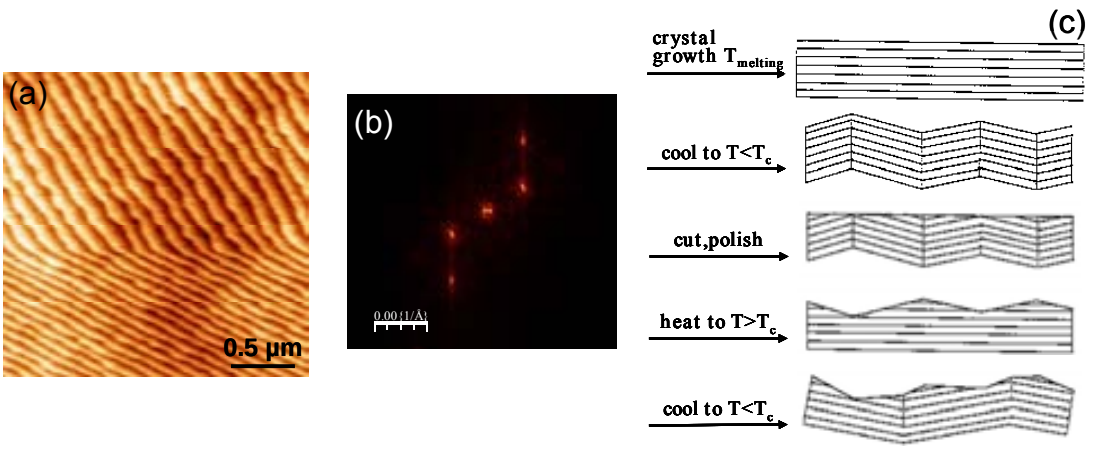

Fig. 3-9: Steps' orientation and terraces' width change at twin boundaries in LAO's substrates: AFM topographic image (a), where steps of the upper side of the twin boundary are ~143 nm width whereas steps of the bottom side are ~75 nm width as determined from 2D-FFT (b). Schematic illustration of the mechanism leading to this phenomenon (c) [175].

3.2 Chemical Solution Deposition (CSD): experimental procedure

Interest and characteristics of CSD have already been revised in section 1.4. In this section, we will describe the experimental procedure followed for the generation of interfacial oxide nanoislands and for the growth of YBCO thin films from chemical solutions.

The coating of the substrate was done by spin-coating, both for the case of interfacial nanostructures and for the growth of epitaxial thin films. In order to minimize the influence of environmental humidity, deposition was carried out in a closed box where N_2 flow permitted to keep the absolute humidity below 2.9 g/m^3.

3.2.1 Preparation of interfacial oxide nanostructures by CSD

We mainly investigated the formation of interfacial nanostructures of the oxide phases $BaZrO_3$ and $Ce_{1-x}Gd_xO_{2-y}$, though some preliminary studies were also carried out with La_2O_3. Accordingly, two previous phases will be more extensively described. The two former phases have been widely studied in our group as buffer layers for multilayer superconductor structures [97, 181-183]. Thus, the synthesis routes and conditions for epitaxial growth of these thin films on similar structure substrate (perovskite on perovskite, fluorite on fluorite) were investigated and optimized prior to this work [184, 185].

3.2.1.1 Precursor solutions of $BaZrO_3$, CeO_2, $Ce_{0.9}Gd_{0.1}O_{2-y}$ and La_2O_3

3.2.1.1.1 Synthesis of $BaZrO_3$ precursor solution

$BaZrO_3$ (BZO) is an oxide with perovskite-type (A=Ba, B=Zr) crystal structure with lattice parameter 4.193 Å. BZO-precursor solution was prepared under atmospheric conditions from precursor compounds barium acetate $Ba(CH_3COO)_2$ (Alfa Aesar) and zirconium acetylacetonate $Zr(CH_3COCHCOCH_3)_4$ (Alfa Aesar). They were dissolved in stoichiometric proportions in glacial acetic acid (Panreac), and stirred and heated at 40°C for 30 min. The resulting solution was filtered to avoid the presence of inclusions larger than 20 μm. This solution is stable for less than a week and, thus, it was prepared prior to each deposition.

Since highly diluted solutions were required for the generation of nanostructures, 0.03 M solutions were initially prepared and, then, they were diluted in glacial acetic acid till the desired concentration so that precision on the weight of precursor compounds was ensured. BZO solution of 0.003M has a viscosity of 1.29 mPa·s and exhibits a contact angle $\gamma \sim 0.3^o$ (Fig. 3-10). Thus, good wetting of substrate during spin coating process was achieved.

Fig. 3-10: Picture showing the wetting of a 0.003 M BZO-precursor solution on a (001)STO single-crystal substrate.

3.2.1.1.2 Synthesis of CeO_2 precursor solution

Cerium oxide exhibits cubic fluorite structure with lattice parameter 5.411 Å. In the fluorite structure, cations (Ce^{4+}) are located at the face centre positions and anions (O^{2-}) are located at the tetrahedral positions of the corresponding faced centred cubic (FCC) lattice formed by the cations. CeO_2 unit-cell and planar-views of (001) and (011)-CeO_2 planes are depicted in Fig. 3-11 using the solid spheres model.

CeO_2 precursor solution was prepared by dissolving a determined quantity of cerium (III) acetylacetonate hydrate $Ce(CH_3COCHCOCH_3)_3 \cdot xH_2O$ (Alfa Aesar) in glacial acetic acid (Panreac). A yellow and transparent solution was obtained after 30 min stirring at 60°C. Fast aging (several hours) of the solution was slightly improved (till one week) by adding 10% in volume of distilled water [185]. Long-term stability (up to several months) was achieved by replacing glacial acetic acid by propionic acid CH_3CH_2COOH and anhydrous isopropanol $(CH_3)_2CHOH$ [184], since these solvents provide more solubility to $Ce(CH_3COCHCOCH_3)_3$ because they have an extra carbon in the hydrocarbon chain.

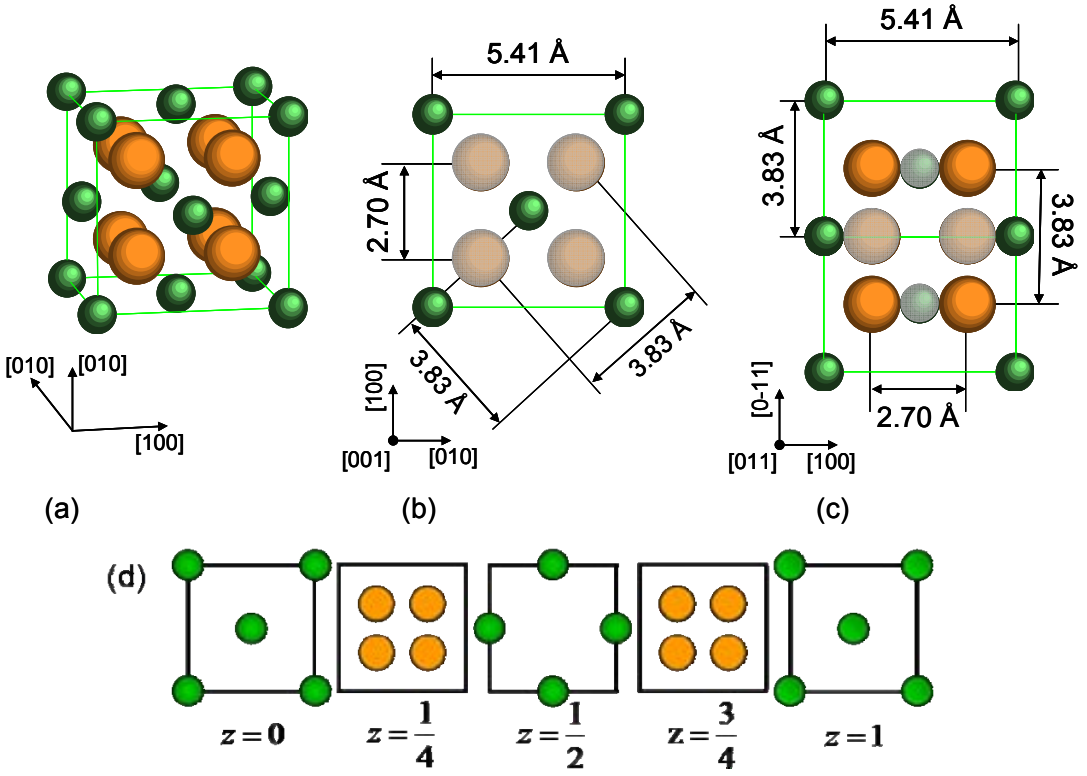

Fig. 3-11: Solid spheres model showing the fluorite unit-cell of CeO_2 (a); planar-views corresponding to CeO_2 planes (001) (b) and (011) (c); and representation of fluorite structure in z-notation (d). Green spheres correspond to Ce^{4+} cations, orange ones refer to O^{2-} anions and grey atoms indicate that they are below the observed plane. The ionic radius in first three sketches is reduced by 40% for better visualization; the last is not done to scale.

Precursor solutions of 0.25 M were initially prepared and then dissolved till the working concentration in the corresponding solvent. 0.0025 M solution prepared from glacial acetic acid has a viscosity of 1.70 mPa·s and wetting angle $\gamma \sim 4^{o}$. Similitude between these values and those typically obtained for 0.003M-BZO precursor solution indicates that rheological parameters of these highly diluted solutions are mainly determined by the properties of the solvent.

3.2.1.1.3 Synthesis of $Ce_{0.9}Gd_{0.1}O_{2-y}$ (CGO) precursor solution

Doping of CeO_2 with Gd^{3+} was carried out to enhance the atomic mobility through the generation of oxygen vacancies in the fluorite structure. Particularly, 10%-Gd doping was proved to significantly improve the epitaxial quality of CSD $Ce_{1-x}Gd_xO_{2-y}$ (CGO) thin films grown on yttria-stabilized zirconia (YSZ) [97, 184]. Ionic radius of Gd^{3+} (1.05 Å) is just slightly larger than that of Ce^{4+} (0.97 Å). Thus, the lattice parameter of CGO (5.411 Å) is nearly the same of CeO_2 (5.410 Å), and the fluorite structure is maintained. Hence, from a structural and size point of view Gd-doping does not distort the system.

For the preparation of 2 ml CeO_2-10%Gd solution, dopant precursor gadolinium acetylacetonate $Gd(CH_3COCHCOCH_3)_4$ (Aldrich) was dissolved in 1 ml of propionic acid

(Aldrich) and 1 ml of isopropanol (Aldrich). This solution was stirred and heated (40°C) for 15 minutes. Then, a stechiometric amount of $Ce(CH_3COCHCOCH_3)_3$ was added and the solution was stirred at 40°C for 30 minutes more. Like previous case, a 0.25 M precursor solution was initially prepared and then filtered and diluted in propionic acid and isopropanol 1:1 till the desired metal concentration.

3.2.1.1.4 Synthesis of La_2O_3 precursor solution

There is certain controversy about the crystallographic structure of La_2O_3. It is generally reported that at low temperature it exhibits a cubic structure with lattice parameter 11.33 Å, whereas at high temperature it displays hexagonal lattice with a_o=3.498 Å and c_o=6.403 Å .

La_2O_3 precursor solution was prepared by dissolving lanthanum (III) acetylacetonate hydrate $La(CH_3COCHCOCH_3)_3 \cdot xH_2O$ in ethanol, and then stirring for 30 min at 50°C. Due to dissolution difficulties, in this case the ultradiluted solution was directly prepared.

3.2.1.2 Deposition and crystallization

Once the corresponding precursor solution was prepared, spin coating was carried out. Using a micropipette, 14 µl were deposited on the chosen single-crystal substrate previously heat-treated according to process described in section 3.1.1. Then, the spin rate was increased from 0 up to 6000 rpm in 2 seconds. This angular speed was held for 2 minutes to ensure homogenous coverage of the substrate.

After spin coating, the samples were heat treated. One-step process was used to transform the as-deposited film into epitaxial interfacial nanostructures. General schematic representation of the heat treatment profile is shown in Fig. 3-12; it was carried out in tubular furnaces. Let's notice that the decomposition of metal-organic precursors typically occurs within the temperature range 300-400°C [100]. We started with the growth conditions previously optimized in our group for the CSD-growth of the corresponding oxide thin films [184, 185]. For BZO, as-deposited films were heated to 900°C at 200°C/h for 4 hours in oxidizing atmosphere. As-deposited CeO_2 layers were treated at 1000°C for 8 hours in oxidizing atmosphere, whereas for CGO films better epitaxiality was achieved when annealing was performed in reducing atmosphere (1000°C, 8 h); in both cases, a heat ramp of 1500°C/h was followed. These initial parameters (temperature, atmosphere, time) were modified to study and control the formation of the corresponding self-assembled oxide nanostructures, as will be presented in chapter 4. The initial heating ramps were maintained; and for La_2O_3 we also used 1500°C/h.

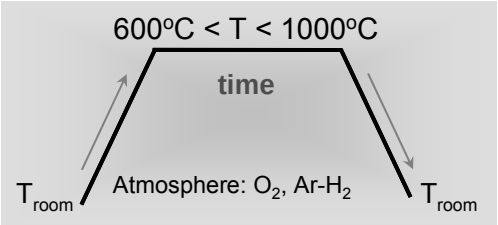

Fig. 3-12: General schema of the thermal treatment followed for the growth of interfacial nanostructures of BZO, CeO_2, CGO and La_2O_3.

3.2.2 Synthesis of $YBa_2Cu_3O_7$ (YBCO) thin films by CSD

From all distinct strategies to prepare superconducting YBCO thin films, CSD-MOD arises as a very competitive strategy to obtain high quality films with controlled microstructure [98, 133, 186]. Companies such as American Superconductor, SWCC Showa holdings, Zenergy Group or Nexans Superconductors are already using MOD for long-length tape production. To date, best results have been achieved using trifluoroacetate precursors (TFA). After metal-organic decomposition, TFA precursors leads to the formation of BaF_2 instead of $BaCuO_2$, which requires high temperatures to decompose leading to the subsequent degradation of final microstructure and superconducting properties of the film [187]. In addition, BaF_2 controls the growth rate of the YBCO film.

The preparation of MOD-TFA thin films is based on all steps of a typical CSD process. The transformation of the as-deposited film to the crystalline YBCO phase is complex; the chemical reactions that take place during pyrolysis (1) and crystallization (2) once the solvent is evaporated can be summarized as:

$$(1)\quad Y(CF_3COO)_{3\,(S)} + 2Ba(CF_3COO)_{2\,(S)} + 3Cu(CF_3COO)_{2(S)} \xrightarrow{H_2O,\,O_2} YF_{3(S)} + 2BaF_{2(S)} + 3CuO_{(S)} + 6CF_3COF_{(g)} + 4COF_{2\,(g)} + 3CO_{2\,(g)} + 7CO_{(g)}$$

$$(2)\quad Ba_{1-x}Y_xF_{2+x\,(S)} + CuO_{(S)} \xrightarrow{O_2,N_2-T\uparrow} Y_2Cu_2O_{5\,(S)} + Y_2O_{3\,(S)} + BaF_{2(S)} \xrightarrow{O_2,N_2,H_2O} YBa_2Cu_3O_{7(S)} + HF_{(g)}$$

In subsequent sections, general features about precursor solution and YBCO thin film growth are reviewed.

3.2.2.1 Synthesis of YBCO precursor solution

TFA-MOD processes using water-content precursors might lead to the degradation of critical current densities of the resulting YBCO thin films. To overcome this drawback, a variation of this process was developed at ICMAB based on the replacement of trifluoroacetatic

acid (TFAH) by trifluoroacetic anhydre (TFAA) [188]. Accordingly, YBCO precursor solution preparation consists of the dissolution of stechiometric commercial YBCO powder (Solvay) in TFAA (Aldrich) together with small amount of TFAH (Aldrich) as catalyst. The mixture is stirred 72 hours at 50^{o}C, and the resulting solution is filtered and evaporated under vacuum. As a result, a mixture of TFA salts ($Ba(TFA)_2$, $Cu(TFA)_2$ and $Y(TFA)_3$) is obtained, which is stechiometrically dissolved in methanol (Aldrich) to get the desired concentration of metals. YBCO precursor solution was prepared by members experts of our group. Typically, precursor solution concentration of 1.5 M was used to grow ~275 nm thick YBCO films.

3.2.2.2 Deposition

According to the goal of this work, deposition was carried out on interfacial nanostructured oxide templates, but also on surface-treated single-crystal substrates used as control samples. In both cases, substrates were cleaned prior to deposition in methanol and acetone in ultrasonic bath and dried with compressed N_2.

Deposition was carried out by spin coating. 14 μl of the precursor solution were deposited on the substrate with a microsyringe. Then, the sample was accelerated in 1 second till the angular velocity of 6000 rpm at which it remained 2 minutes. After deposition, samples were submitted to a heat treatment which can be separated in the three stages described next.

3.2.2.3 Pyrolysis, growth and oxygenation

The precursor film was decomposed in humid O_2 atmosphere accordingly to the heat profile schematized in Fig. 3-13. High control over pyrolysis is critical since during this process occurs a strong reduction of the layer volume (70-80%), which may lead to the generation of cracks or other undesired effects.

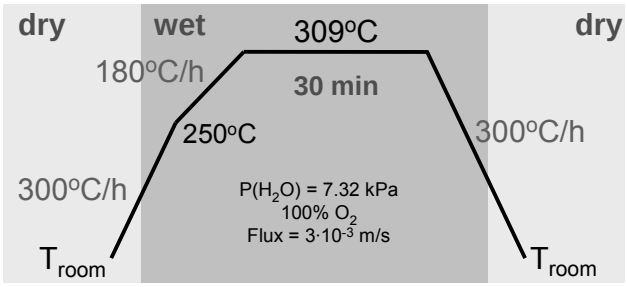

Fig. 3-13: Temperature heating profile used in pyrolysis of MOD-TFA YBCO thin films.

In a second heating step, the pyrolyzed film is heated up to 810^{o}C under a wet atmosphere composed by oxygen and nitrogen to crystallize in the tetragonal phase of YBCO. The exact thermal profile followed at ICMAB is schematized in Fig. 3-14 (first part of profile).

A wet atmosphere is required to convert the BaF_2 pyrolysis product into HF, which is evacuated by gas flow. As decomposition of BaF_2 proceeds, YBCO nucleation takes place at substrate interface. Thus, YBCO growth rate depends on water pressure, oxygen pressure, rate of gas flow and temperature.

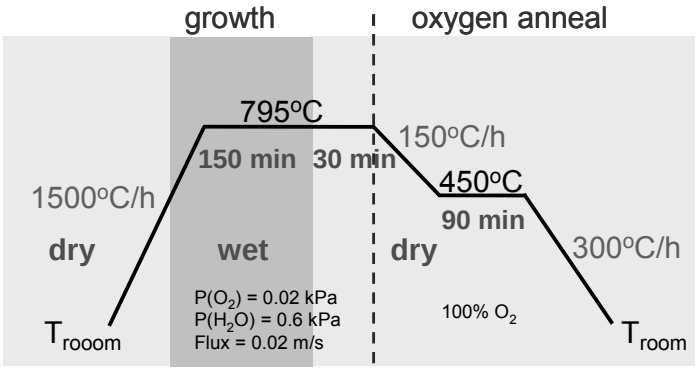

Fig. 3-14: Schematic profile of MOD-TFA YBCO growth and oxygenation processes.

Finally, the YBCO thin film is oxygenated at 450ºC (second part profile in Fig. 3-14) under O_2 atmosphere to convert the tetragonal YBCO phase into the superconducting orthorhombic YBCO phase.

Chapter 4

Interfacial oxide nanostructured templates

The spontaneous formation of interfacial nanoislands as a mechanism of elastic relaxation during lattice mismatched heteroepitaxial growth is generally accepted [15]. Therefore, misfit between the two present materials arises as an important driving force for the growth of interfacial epitaxial nanostructures. For example, it has been observed in semiconductor materials that strain not only may drive the transition from 2D to 3D nanoislands, but can also determine and influence its shape transition, resulting in a complex evolution of the island itself and of the whole ensemble [31, 189, 190]. However, the change in surface energy due to island's formation may also play a key role. It is normally assumed that surface energy implies an extra energetic cost that the system must pay when decreasing its elastic energy through island creation [12, 60, 191]; but this fee actually depends on the particular energy of facets and interface of the grown nanostructure [15]. Hence, the formation of an interfacial island is a complex phenomenon essentially based on a trade-off between surface and interface energies and elastic relaxation energy.

Nonetheless, it must be taken into account that kinetic mechanisms are also involved in the evolution of the system and, particularly, in heteroepitaxial systems, misfit can change the thermodynamics of the equilibrium structures but also the kinetics of the system. In general, kinetic phenomena can act helping to achieve the lowest energy configuration of the system or, inversely, keeping interfacial nanoislands far from their configuration of thermodynamic equilibrium [15]. Kinetic processes are strongly related to the atomic mobility of the specimen; that is, linked to atomic diffusion. Therefore, in addition to misfit, nanostructures' formation and evolution can also be controlled and modified through growth parameters such as temperature, atmosphere or time of annealing. So, by stopping the system during corresponding heat treatment, it is possible to access the intermediate stages of evolution followed by nanostructures before achieving their final equilibrium structure.

Under the appropriate conditions, the combination of all these phenomena (compensation between elastic and surface energy, and kinetic mechanisms) can drive the

system to the spontaneous formation of uniform nanostructures with a narrow distribution of sizes. A further step may take place when these self-assembled nanoislands also self-organize. As a result, highly ordered templates can be achieved just leaving the system evolve to the minimum energy configuration, as simple as nature does.

Additionally to the fact that strained layers are inherently unstable and tend to create islands, the formation of 3D nanostructures can also be enhanced by limiting the amount of deposited material. Being the growth mechanism highly dependent on the growth technique, one may mainly achieve the generation of nanostructures through two possible paths: the induction of instabilities in continuous heteroepitaxial films [87, 110] or the control of nucleation processes when very small quantities of material are deposited [77, 92], which for the particular case of chemical solution deposition (CSD) is equivalent to use highly dilute solutions, as presented in the introductory chapter. First approach generally leads to the growth of larger structures, typically within the range of 100 nm, making it a priori less suitable for the preparation of templates with high density of nanostructures. Therefore, within the frame of the present work we focus on the generation of interfacial oxide nanostructures from highly diluted chemical solutions.

In this chapter, we present an overview of the influence of lattice mismatch, precursor solution concentration and growth parameters (atmosphere, temperature and annealing time) on the mechanisms of nucleation and growth of self-assembled interfacial oxide nanostructures ($BaZrO_3$ (BZO), $Ce_{1-x}Gd_xO_{2-y}$, La_2O_3). As substrates, perovskite ABO_3 single-crystals ($SrTiO_3$ (STO), $LaAlO_3$ (LAO)) were used, all them previously thermally treated in oxidizing atmosphere to ensure atomically flat terraces separated by one unit-cell high steps (see also chapter 3). Nanostructures were prepared from chemical solutions, which were homogeneously spread over the substrate by means of spin-coating. Taking into account that concentrations of $\sim 10^{-1}$ M are typically used for the growth of continuous thin films, solutions of about 10^{-2}-10^{-3} M were considered to promote the formation of nanostructures. Such concentrations were initially used for a first scan of the influence of growth parameters on interfacial nanostructures formation; though, later, optimization of solution concentration was carried out.

4.1 Strain-induced oxide nanoislands

Due to the important role that misfit between the deposited material A and the substrate B plays in heteroepitaxial growth, it is an important aspect to consider when studying the generation of interfacial nanostructures. To compute the degree of lattice mismatch between two structures, one calculates the relative difference between the interatomic distances more

favourable for epitaxial growth. For the growth of high quality epitaxial oxide films on oxide substrates, it has been generally observed that the misfit and crystal symmetry of the oxygen sublattices is more important than that of the cation sublattice itself [192]. Thus, lattice mismatch between two oxide structures is defined through the coincidence lattice site model [193] as

$$\varepsilon = \frac{x_{substrate} - x_{layer}}{x_{layer}} \qquad \textbf{Eq. 4-1}$$

where x_{layer} refers to the interatomic oxygen-oxygen distance of the deposited material that better fits the oxygen-oxygen distance of the substrate ($x_{substrate}$). If $x_{substrate}$ is larger than x_{layer} ($\varepsilon>0$), the resulting strain is tensile; and if $x_{substrate}$ is smaller than x_{layer} ($\varepsilon<0$), the strain is compressive. The former corresponds to a surface which favours contraction, whereas the latter is associated with a surface that favours expansion.

Table 4-1: Summary of lattice parameters and matching distances of substrates and oxide structures used.

Material	Structure	Lattice parameter (Å)	Matching distance (Å)	Misfit to $LaAlO_3$ (%)	Misfit to $SrTiO_3$ (%)
$LaAlO_3$	pseudocubic/perovskite	3.79	3.79	0	3.17
$SrTiO_3$	cubic/perovskite	3.91	3.91	-3.07	0
$BaZrO_3$	cubic/perovskite	4.19	4.19	-9.55	-6.68
CeO_2	cubic/fluorite	5.41	5.41 d(100)	-29.94	-27.73
			3.83 d½(110)	-1.04	2.09
La_2O_3	cubic	11.33	4.01 d¼(110)	-5.49	-2.49
	hexagonal	a_o=3.49	3.49	8.59	12.03
		c_o=6.40	3.20 d½(001)	18.44	22.19

Consistently with this model, perovskite BZO is expected to grow cube-on-cube on the also perovskite STO single-crystal with the crystallographic relation (001)BZO[100]||(001)STO[100], which has a lattice mismatch of $\varepsilon_{BZO/STO}$= -6.68%. Thus, BZO growth on STO takes place under compressive strain. CeO_2/LAO system corresponds to the growth of a fluorite structure on a perovskite substrate. For the epitaxial relation (001)CeO_2||(001)LAO, the oxygen sublattices are very well matched provided that one cube is rotated 45^o around [001] axis with respect to the other, i.e. (001)CGO[110]||(001)LAO[100]. The oxygen sublattice constants of 3.83 Å along [110]-CeO_2 and 3.79 Å along [100]-LAO also result into a compressive lattice mismatch of $\varepsilon_{CeO2/LAO}$ = -1.04%. This configuration is due to the face centred cubic packing of cations in CeO_2 fluorite. For both systems and suggested epitaxial crystallographic relations, the lattice misfit between deposited material and substrate is less than 7-8%. Therefore, conventional models of lattice epitaxy can be considered; otherwise, it should be used the domain matching model to explain the epitaxial growth of large mismatched

systems [194]. Matching distances corresponding to distinct oxides used through the present work are compared in Table 4-1.

With the purpose of illustration, Fig. 4-1 shows two typical cases of surface instabilities that can be induced in the above described systems, BZO/STO and CeO_2/LAO, when equivalent thickness of less than a few nanometres are deposited. Despite growth conditions (temperature, oxygen pressure and annealing time) are fairly similar, differences in morphology, size and density between interfacial BZO and CeO_2 nanostructures unambiguously stand out.

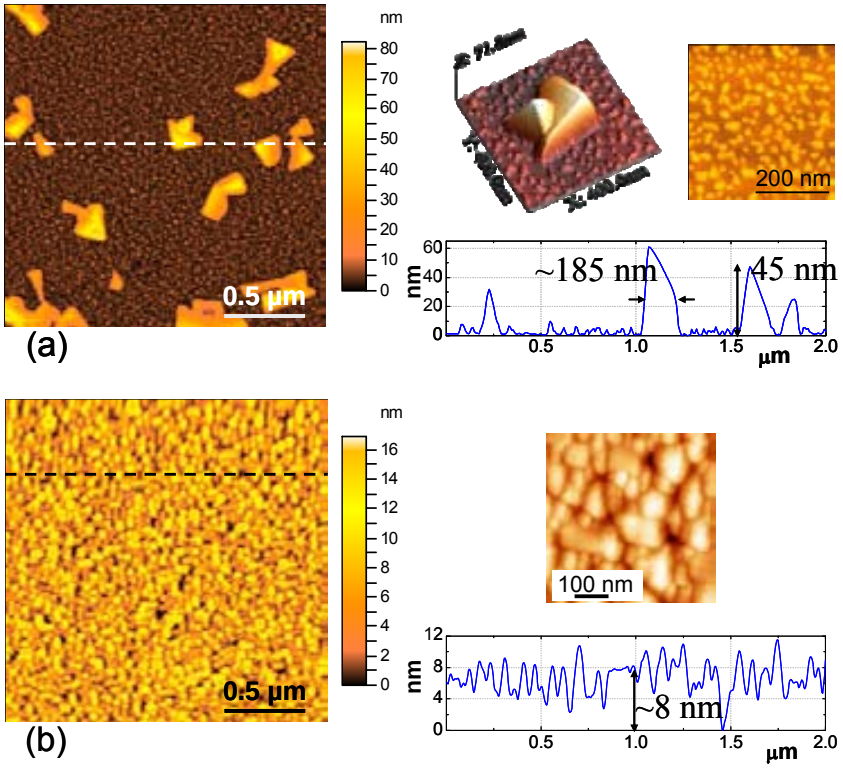

Fig. 4-1: Topographic AFM images of interfacial nanostructured BZO/STO (a) and CeO_2/LAO (b) templates. The former was prepared from 0.03M precursor solution and processed 4 h at 900°C in O_2; the latter was prepared from 0.025M precursor and treated 8 h at 1000°C in O_2.

Fig. 4-1a shows a topographic AFM image of a nanostructured BZO/STO template obtained after the deposition of 0.03M BZO precursor solution on a (001)STO single-crystal substrate. Heat treatment was carried out at 900°C for 4 hours at 1 bar oxygen pressure with a flux of ~0.03 l/min. A bimodal distribution of sizes of interfacial BZO nanostructures is observed. Large irregular polyhedral islands (population 1) with mean size ~185 nm, mean height ~45 nm and mean density of 4 nanoislands/µm^2 are observed. Additionally, smaller nanodots of ~18 nm lateral size and ~4 nm average height are also distinguished in the background (population 2). The origin of this bimodal distribution is not well established, but it is very likely that a competition between nucleation and coarsening leads to such a structure. These BZO/STO templates prepared from 0.03M precursor solutions and processed 4 h at

900ºC in O_2 are taken as reference in subsequent studies, where the influence of solution's concentration and growth conditions on this system is investigated.

In Fig. 4-1b, a typical example of a CeO_2/LAO nanostructured template prepared from a precursor solution 0.025M is presented. The crystalline growth was carried out at 1000ºC, in oxidizing atmosphere during 8 hours. These templates display a nearly compact coverage of the LAO substrate with homogeneous parallelepiped nanostructures of lateral size ~100-140 nm and mean height ~10 nm. This morphology is similar to that reported for CeO_2 thin films grown on sapphire by magnetron sputtering [195].

Comparing both templates, it is clearly illustrated that in heteroepitaxial growth the lattice mismatch promotes the formation of 3D nanoislands as a mechanism of elastic relaxation in heteroepitaxial growth. Large interfacial 3D nanostructures grow for highly mismatched systems, as exemplified by the system BZO/STO with $\varepsilon_{BZO/STO} \sim -7\%$. However, for small misfits (i.e. $\varepsilon_{CeO2/LAO} \sim -1\%$) interface energy is expected to be lower, which may allow a growth mode closer to a layer-by-layer approach. Accordingly, an almost complete coverage of LAO substrate with parallelepiped CeO_2 nanostructures is observed. Differences in morphology, size and density between these nanostructures suggest that not only the thermodynamic equilibrium shape seems to differ between both systems, but also the kinetics of ripening and coalescence leading to the formation of the corresponding interfacial nanoislands.

In subsequent sections, the particular characteristics of these interfacial oxide nanostructures are discussed in relation to selected growth parameters (atmosphere, temperature, time). First part is devoted to BZO/STO system, and second one refers to $Ce_{1-x}Gd_xO_{2-y}$/LAO. Some examples of La_2O_3 nanoislands grown on LAO substrates are as well reported at the end.

4.2 Interfacial $BaZrO_3$ nanostructures

Due to its physical and chemical properties, $BaZrO_3$ (BZO) is a material of relevance with applications in multitude of fields ranging from its use in fuel cells to aerospace industries [196-198]. Although till the moment most of BZO applications are associated to its bulk, powder or thin film form, the generation of nanostructures may spread these possibilities from common uses to advanced technologies. In fact, interesting results in research associated to unique and new properties of perovskite crystal structures at reduced scale are being reported [160, 199-201]. For example, BZO has been identified as a unique second phase for improvement of vortex pinning at high temperatures and high magnetic fields [140, 142, 144].

4.2.1 Effect of growth atmosphere

The transport of mass by atomic mobility (i.e. diffusion), and thus kinetics of nanostructures, is generally strongly dependent on the atmosphere in which the sample is processed, i.e. oxygen pressure in the case of oxide materials. This behaviour is explained through the generation of vacancies in the crystalline structure, which enhances atomic mobility [202]. Vacancies are lattice sites of the crystallographic structure which are unoccupied by atoms. They are point defects, and they constitute the most elementary defects. They are a common phenomenon, especially at high temperatures when atoms change frequently and randomly their positions leaving behind empty lattice sites. The fraction f of unoccupied sites with respect to the total number of sites as function of temperature is estimated by [203]

$$f = \exp\left[-\frac{E_f}{K_B T}\right] \qquad \textbf{Eq. 4-2}$$

where E_f is the energy required to remove an atom from an interior site and place it on the surface. If a neighbouring atom moves to occupy a vacant site, the vacancy moves in the opposite direction to the site which used to be occupied by the moving atom. In many cases, diffusion can actually occur because of vacancies. In oxide materials, missing oxygen atoms at the expected lattice site are a common vacancy. Hence, the amount of oxygen vacancies in oxides can then be modified through the oxygen pressure during growth and posterior annealings.

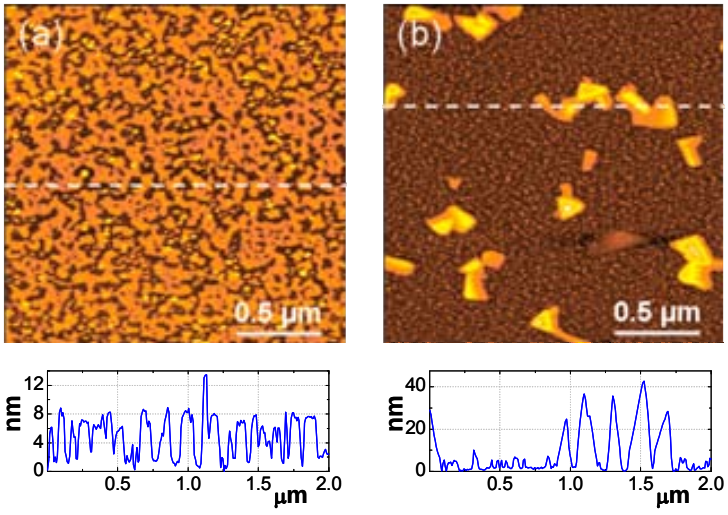

Fig. 4-2: Influence of oxygen pressure on BZO/STO system. AFM images and corresponding profiles of templates processed in Ar-5%H_2 (a) and O_2 (b) atmosphere for 4 h at 900°C. Both samples were prepared from 0.03 M precursor solution.

To study this influence, two samples were prepared from the same precursor solution concentration (0.03 M) and at the same temperature and annealing time (900°C, 4 h), but in different oxygen pressures, O_2 and Ar-5%H_2. A pure oxygen atmosphere corresponds to P(O_2)

= 1 bar, whereas in reducing atmosphere of Ar-5%H_2 an oxygen pressure below $P(O_2) = 10^{-15}$ would be reached. Fig. 4-2 shows the corresponding topographic AFM images of the resulting BZO/STO templates. Templates grown in Ar-H_2 atmosphere (Fig. 4-2a) exhibit a high degree of substrate coverage with rounded and connected elongated structures of about (7±2) nm high. Embedded in this matrix, few nanodots of just ~20 nm in diameter and ~9 nm in height start to be distinguished.

Fig. 4-2b corresponds to the partner sample grown in O_2. It is equivalent to template already reported in section 4.1. Polyhedral BZO nanoislands (population 1) with ~185 nm mean size, ~45 nm mean height and density of about ~4 islands/μm^2 outcrop from a background of homogeneously distributed small nanodots (population 2). Further details of this bimodal size distribution are revealed by TEM studies. Fig. 4-3a exhibits a low magnification TEM planar-view image, where the pronounced bimodal distribution is appreciated. A higher magnification TEM image (Fig. 4-3b) shows that the population of small nanostructures on the background actually consists of clusters of smaller particles instead of compact irregular nanoislands, as was derived from AFM images. Several details of BZO nanoislands in population 2 are shown in TEM images in Fig. 4-3c,d and e. Sharp linear dark and bright contrasts in TEM images in Fig. 4-3 are bend extinction contours which arise from slight local variations of the diffraction conditions related to curvature effects of the substrate and, thus, they are independent of the film microstructure.

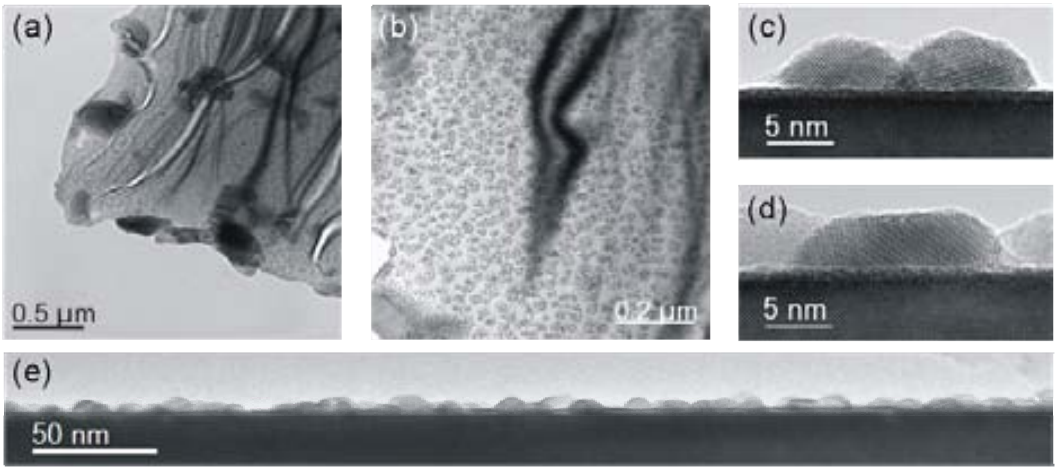

Fig. 4-3: TEM images of a reference BZO/STO template (0.03M; O_2, 900°C, 4 h): low magnification planar-view image showing the bimodal size distribution of BZO nanoislands (a); high magnification planar-view image revealing the formation of clusters of nanodots at the background with homogeneous spatial and size distribution (b); high (c,d) and low (e) resolution cross-section images of the background nanodots (population 2). Dark and bright lines contrasts are bend extinction contours not related to the microstructure of the sample.

Differences between samples treated in Ar-H_2 and O_2 suggest that a further evolution stage is reached in oxidizing atmosphere. Whereas well-defined polyhydral BZO nanoislands (population 1) form in O_2, the nucleation of the first events just starts to take place in Ar-5%H_2

reducing atmosphere for the same period of heat treatment. These strong differences evidence the important role that growth atmosphere can play on atomic diffusion [204]. From presented results, it can be state that high oxygen pressure enhances BZO atomic mobility in comparison with a reducing one. The mechanism steering this behaviour is unknown at present, though it could be related to the protonic conductivity of BZO [196, 205]. Ar-H_2 atmosphere could alter BZO structure through aliovalent doping ($BaZr_{1-x}M_xO_{3-y}$ where M=Y, K [206, 207]) and, as a result, the atomic mobility of the system might decrease.

4.2.1.1 Influence of atmosphere on the evolution of BZO nanostructures

Differences observed in atomic mobility of BZO nanostructures on (001)STO substrates resulting from distinct oxygen pressure are preserved after longer annealings. Shots of the evolution path followed by templates treated in Ar-H_2 at 1000°C for periods ranging from 4 to 16 hours are shown in Fig. 4-4. Till heat treatments as long as 12 hours, no significant differences are observed with respect to templates described in previous section 4.2.1, i.e. few and small nanodots outcrop from an amorphous background of snake-like interconnected structures which covers all the substrate. From 16 hours treatments and so, a bimodal size distribution arises similar to that observed in BZO/STO samples just treated in oxidizing atmosphere for 4 hours. After 16 h anneal, Ar-5%H_2 nanoislands of population 1 are ~(260±80) nm in equivalent diameter and have an mean height of ~71 nm; their density is of just 0.6 islands/μm^2. Mean size of nanoislands' constituting population 2 is difficult to determine within AFM resolution limits; a mean height of ~11 nm is observed. Thus, the slow mobility of BZO nanostructures in Ar-H_2 reducing atmosphere with respect to those treated in high oxygen pressure is confirmed.

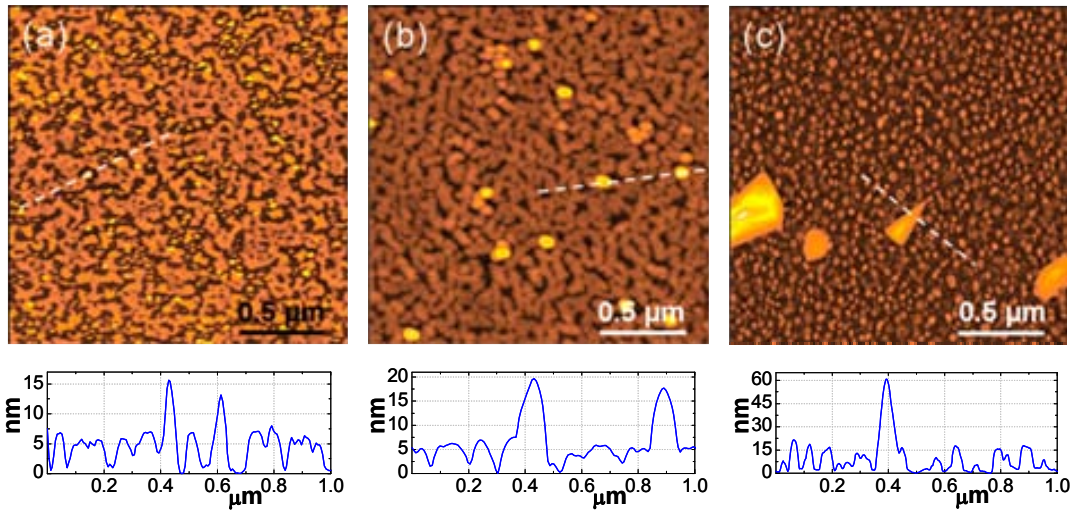

Fig. 4-4: Evolution of BZO/STO templates in reducing atmosphere: 4 h (a), 12 h (b) and 16 h (c). Samples were annealed at 900°C and prepared from 0.03M precursor solutions.

Samples annealed in oxidizing atmosphere show a bimodal distribution for all investigated treatment times, i.e. till 50 h (Fig. 4-5a to d). Large nanostructures constituting population 1 increase in size and height as anneal proceeds and, simultaneously, the number of islands per unit area slightly decreases. The evolution of volume and density of island's in population 1 is plotted in Fig. 4-5e. Coarsening phenomenon, where some islands grow at expenses of others, occurs to probably minimize the total surface energy of the system. However, increase of islands' volume is not only due to the diffusion of atoms within nanoislands of population 1, since the total amount of material constituting these nanostructures also increase with annealing time. Evolution of the total amount of material making up population 1 is shown in Fig. 4-5f through the equivalent thickness parameter, which corresponds to the thickness of a thin film of the same volume occupying the considered template's area. Therefore, a complex coalescence process occurs during annealing, where there is mass transfer from nanostructures of the background (population 2) to the large BZO polyhedral nanoislands (population 1), at the same time that coarsening phenomena also takes place between nanoislands of population 1.

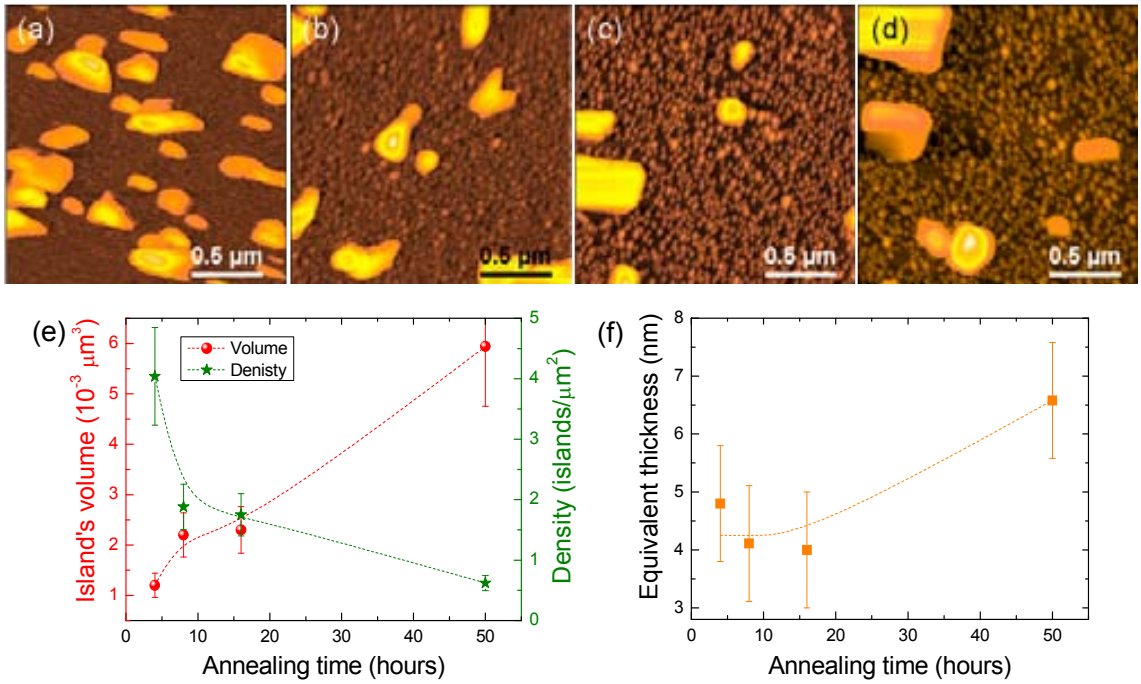

Fig. 4-5: Evolution of BZO/STO templates in oxidizing atmosphere: 4 h (a), 8 h (b), 16 h (c) and 50 h (d). The corresponding change of volume and density (e) and equivalent thickness (f) of islands constituting population 1 is also plotted. All samples were annealed at 900°C and prepared from 0.03 M precursor solutions.

Hence, the atomic mobility of BZO is proved to drastically enhance when it is treated in oxidizing atmosphere in comparison with templates processed in Ar-H_2. Accordingly, due to our interest in the investigation of processes of nucleation and evolution of interfacial BZO nanostructures, from now on we will focus on BZO nanostructures grown in O_2.

4.2.2 Effect of growth temperature

Atoms' diffusion depends on atoms' jump from their present site to a neighbour one. Diffusivity is a thermally activated process which depends on temperature as

$$D = D_o \exp\left(\frac{-Q}{RT}\right) \qquad \textbf{Eq. 4-3}$$

where D_o is a constant and Q an experimentally determined activation energy [202]. Thus, atoms are expected to move faster as higher is the annealing temperature. Moreover, and it has been explained in the introductory chapter, temperature also influences the driving forces that determine nucleation processes. As temperature rises more thermal energy becomes available to surmount nucleation barriers of different kind of events and, thus, distinct populations arise. Thus, temperature plays an important role in both nanoislands' nucleation and evolution.

Consequently, in order to study nucleation processes and minimize coarsening effects, formation of BZO nanostructures at reduced temperature was investigated owing to its influence on atomic mobility. Role of temperature in BZO/STO system was studied through the preparation of equivalent samples (0.03 M, oxidizing atmosphere, 4 h annealing) at different temperatures. Fig. 4-6 shows the results for templates processed at 600ºC (a), 700ºC (b) and 900ºC (c).

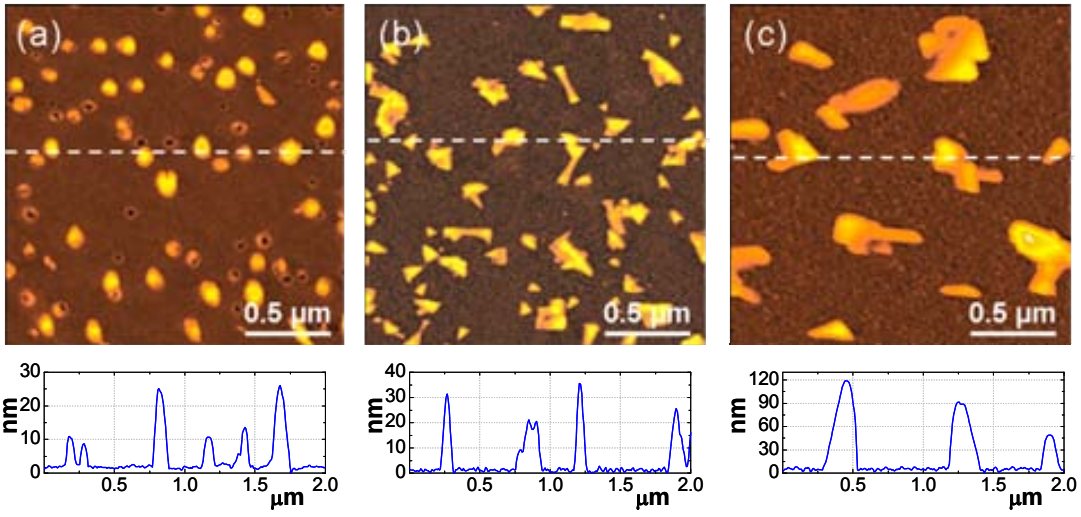

Fig. 4-6: Influence of heat treatment temperature on BZO/STO templates. The AFM topographic images and profiles correspond to samples processed at 600ºC (a), 700ºC (b) and 900ºC (c). All them were prepared from 0.03M precursor solutions, and annealed for 4 h in oxidizing atmosphere.

In templates prepared at 600ºC (Fig. 4-6a), most of deposited material is still constituting the amorphous layer formed after organic decomposition and the nucleation of the first events just starts to take place. The shape of these 3D nanostructures cannot be accurately determined within AFM resolution limits. They have mean equivalent diameter of ~(101±24)

nm and mean maximum height of ~(21±6) nm, and they emerge from the amorphous background with a density of ~10 islands/μm^2. Therefore, these results point out that thermal energy available to the system below and at 600°C is not enough, in general, to overcome the energetic barrier required to transform the amorphous layer to a crystalline structure, at least for the annealing period investigated.

For heat treatments performed at 700°C and higher temperatures, templates show the already described bimodal BZO island's distribution, i.e. population 1 and 2. Differences between polyhedral nanostructures of population 1 of templates prepared at 700°C and 900°C (Fig. 4-6b and c, respectively) are basically in size, suggesting that the nucleation events dominating within this thermal range are mostly the same. Data corresponding to these islands' volumes and densities are plotted in Fig. 4-7a. There exists an increase of the size of islands constituting population 1 as higher is the growth temperature, at the same time that islands' mean density decreases. These differences are mainly attributed to an enhancement of atomic diffusivity with temperature in accordance with relation exposed in Eq. 4-3. As a result, coalescence processes are promoted at high temperatures. Increase of atomic mobility with temperature is in agreement with the highly refracting character of BZO, since this ceramic requires to be treated at very high temperatures, typically ~1500°C, to sinter [208, 209]. Thus, it is expected a low atomic mobility at lower annealing temperatures, which progressively increases as temperatures does. This reduced mobility of BZO is consequence of a low intrinsic concentration of vacancies, which has been proved to increase through aliovalent doping [206, 207, 210].

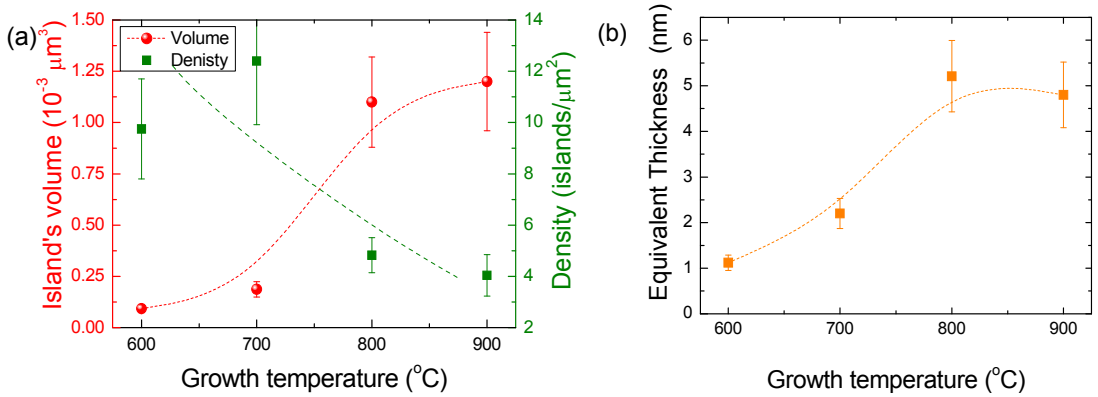

Fig. 4-7: Volume and density as function of annealing temperature of islands in population 1 of BZO/STO templates (a). Equivalent thickness of material constituting this population 1 is also plotted (b). All templates were prepared from 0.03 M precursor solutions and annealed in oxidizing atmosphere for 4 h; corresponding AFM images are displayed in Fig. 4-6.

Furthermore to the augment of mean islands' volume with temperature, there is also an increase of the total amount of material constituting nanostructures in population 1, as displayed in Fig. 4-7b. So, for the same annealing period, more material is removed from the background

as higher is the temperature. Similar evolution path was noted to happen as annealing time progressed at a given temperature (section 4.2.1.1). This tendency is indicative of a kinetically-limited process where ripening occurs based on mass transfer from the background nanodots to the large BZO polyhedral nanostructures, in addition to coalescence phenomena.

These mechanisms of mass transfer clearly distinguish strain-induced nanostructures grown by means of chemical solutions from those prepared using vacuum related techniques. In the former, the final amount of material is present in the sample as an amorphous layer since the beginning of the heat treatment. However, for the latter, material is deposited meanwhile. Other basic differences exist between both deposition routes. Whereas in vacuum related techniques deposition is carried out at fixed substrate temperature, deposition of chemical solutions is done at room temperature and, then, the sample is progressively heated to the growth temperature. Moreover, organic removal dependence with chemistry of the precursor, the solvent used, etc. [100], as well as the pathway leading to the crystallographic structure and its evolution, also distinguish CSD-derived nanostructures from those deposited in vacuum media.

Summarizing, under investigated growth conditions, templates with interfacial BZO nanostructures on (001)STO substrates are a clear example of kinetically-limited processes where complex mass transfer between nanostructures occurs. However, it has been proved that kinetic mechanisms related to atomic diffusion can be improved through temperature and/or annealing period. As higher is the temperature and longer the annealing, an advanced evolution stage is reached.

4.2.3 Effect of solution concentration

The coexistence of two distinct populations of islands makes difficult to model nucleation and growth processes of strain-induced nanostructures. Therefore, BZO/STO templates prepared from lower solution concentrations were investigated. Through the variation of solution's concentration, the final amount of deposited material is also modified, which may influence the size and density of interfacial nanoislands as well as the interaction between them. Notice that reduction of solution concentration in CSD can be compared to shorten the deposition time when vacuum related techniques are used.

With this purpose, a study of BZO-nanostructures formation using different precursor solution concentrations, ranging from 0.03M to 0.003M, was carried out. General tendency of solution's influence is displayed in Fig. 4-8 through templates prepared from precursor solutions of 0.03M (a), 0.006M (b) and 0.003M (c). All samples were processed at 900^{o}C for 4 h in

oxidizing atmosphere. In former sections, these resulted to be the more optimal growth conditions, since high oxygen pressure and high temperatures provide the highest mobility to the system and no large differences were observed for longer annealing periods. Size and density of large nanoislands (populations 1) are summarized in Table 4-2. Accurate size evolution of background nanodots is difficult to determine due to AFM's tip convolution effects.

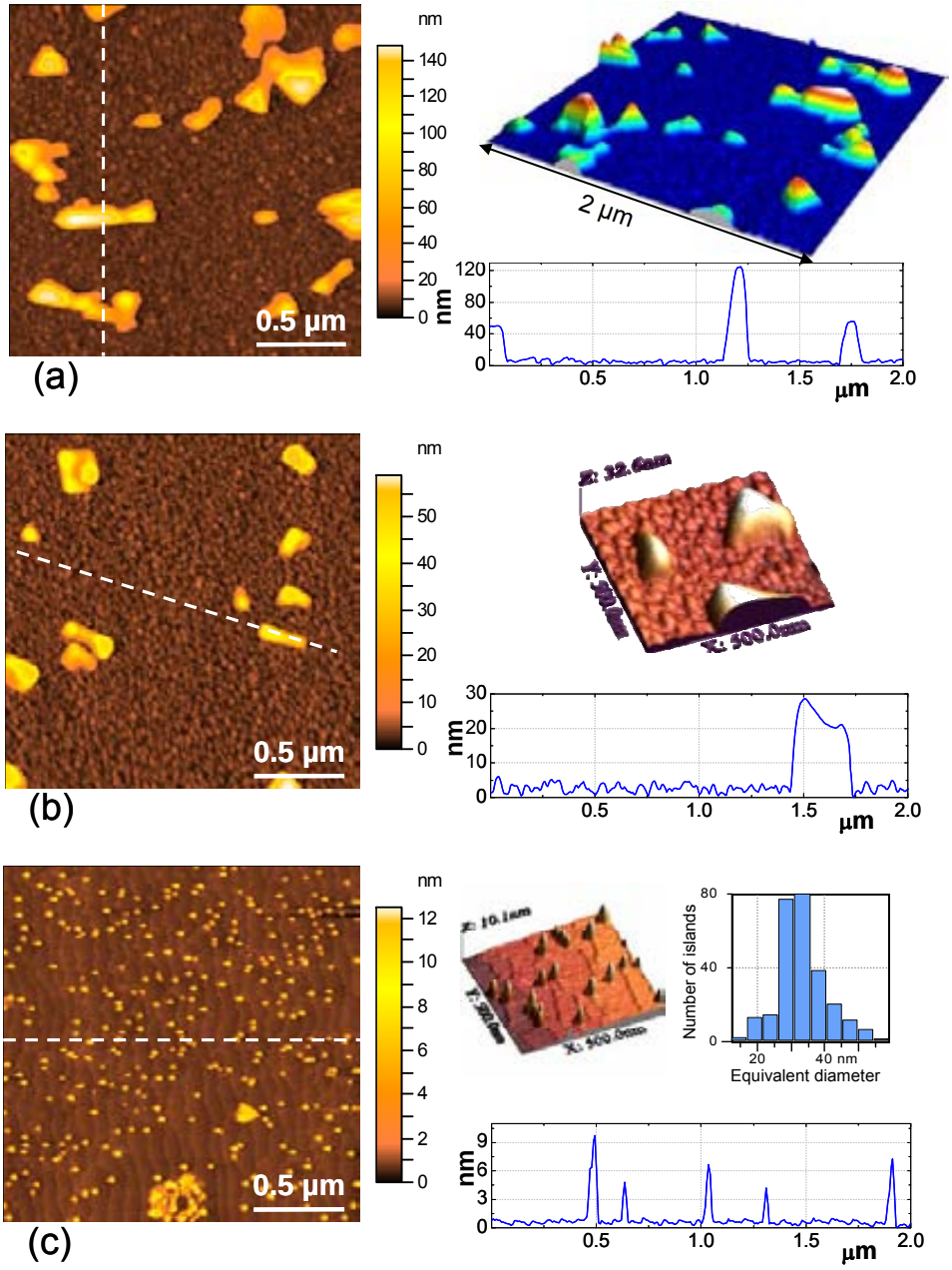

Fig. 4-8: BZO/STO templates prepared from distinct precursor solutions: 0.03M (a), 0.006M (b) and 0.003M (c). All samples were processed at 900°C for 4 h in oxidizing atmosphere.

Fig. 4-8a displays 2D and 3D AFM topographic images of BZO/STO templates prepared from 0.03 M precursor solution, which corresponds to the typical reference example

shown in previous sections. For template exhibit in Fig. 4-8b, BZO precursor solution was diluted in glacial acetic acid till 0.006M. In this case, a bimodal distribution of islands' sizes is still observed: polyhydral BZO islands (population 1) and small nanodots in the background (population 2). However, due to the reduction of deposited material, the mean volume of islands of population 1 decreases ~75% with respect to samples prepared from solution five times more concentrated (Fig. 4-8a). Mean height of background clusters of nanodots (population 2) is ~ 2 nm, which represents about half the height of those in reference sample 0.03M.

Table 4-2: Mean height, equivalent diameter and density of nanoislands in population 1 of BZO/STO templates as function of precursor solution concentration. All templates were annealed in oxidizing atmosphere for 4 h at 900ºC; corresponding AFM images are displayed in Fig. 4-8.

Concentration (M)	Height (nm)	Equivalent diameter (nm)	Density (islands/μm^2)
0.03	45±10	185±90	3.9±1.8
0.006	19±5	147±50	4.7±1.1
0.003	6±1	40±10	59±9

A bimodal distribution of interfacial islands' sizes does not exist any more for template displayed in Fig. 4-8c. It was prepared from a 0.003M precursor solution, which corresponds to ten times more diluted than reference template (0.03M). Just unique size distribution of isolated BZO nanodots with equivalent diameter and height in the range of ~40 nm and ~6 nm, respectively, and a density of ~60 nanodots/μm^2 is observed. These nanodots' mean volume corresponds to an equivalent deposition of about ~ 1 monolayer of BZO. In this template, steps of STO substrate are clearly observed below BZO nanodots.

Hence, size of BZO-nanoislands within population 1 and 2 gets smaller as solution concentration is reduced, as consequence of the diminution of total amount of deposited metals. Particularly, for sufficiently low solution' concentrations, templates with monomodal distributions of sizes are even achieved. Templates with unique size of interfacial BZO-nanoislands are of special interest for many technological applications, as it is the case of quantum dots in semiconductor materials [13]. Moreover, study of the characteristics of these uniform distributions of oxide nanodots prepared by means of chemical solutions is also interesting from a scientific point of view. Therefore, next section is entirely devoted to this sort of templates.

4.2.4 Templates with monomodal distribution of BZO nanodots

Templates with BZO nanodots shown in Fig. 4-8c are a clear example of the existence of self-assembling processes in CSD-prepared interfacial oxide nanostructures, as it is derived

from their narrow size distribution of less than ~15%. Thus, self-assembling mechanisms typically observed when using vacuum growth techniques can also be applied to interfacial oxide nanoislands grown from chemical solutions.

TEM cross-section images show that BZO nanodots have typical sizes between 10-40 nm and heights within the range of 5-15 nm. These dimensions are smaller than those determined from AFM images, where tip convolution effects mask the real size of interfacial BZO nanodots (which exhibit dimensions close to tip dimensions itself). Fig. 4-9a displays a high resolution TEM image of a typical BZO nanodot prepared from 0.003 M precursor solution. In this particular example, BZO-nanodot was grown on a (001)LAO single-crystal substrate (ε~-9.5%) under the same growth conditions previously described; similar nanodots were also observed on STO substrates. A clean sharp interface is observed between the dot and the substrate. BZO nanodots are commonly faceted with {110} and {110}-planes, though more in the former than in the latter. Particularly, the fact that {110} planes are not well-defined (as indicated by the arrows in the figure) could suggest that these lateral sides are actually facetted with (001)-steps. In this case, BZO nanodots would be exclusively faceted with {100} planes, which are the lowest energy surfaces in perovskites [211-213].

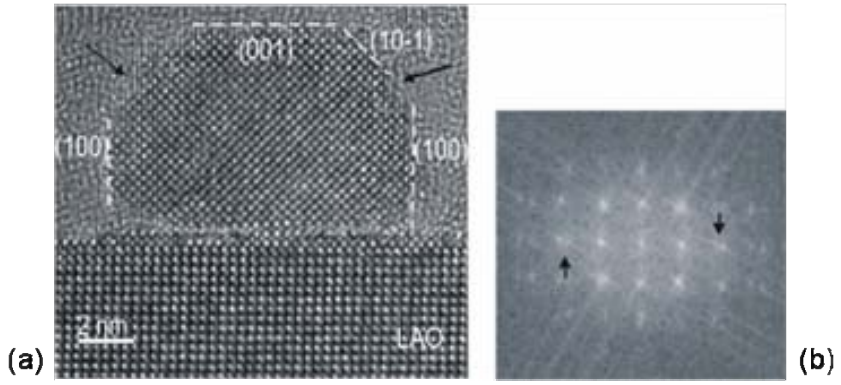

Fig. 4-9: TEM cross-section (a) of a BZO-nanodot grown on (001)LAO substrate, seen along [100] zone axis; and corresponding FFT (b) at the interface where arrows indicate spot splitting associated with in-plane lattice spacings (a). This template was prepared from 0.003 M precursor solution and annealed 4 h at 900^{o}C in oxidizing atmosphere.

TEM images also reveal that BZO-dots exhibit cube-on-cube epitaxial relationship with the substrate, i.e. (001)BZO[100]||(001)STO[100]. This configuration provides the best matching of the oxygen sublattices of both perovskites, BZO and STO, as it is observed in solid spheres model (planar and lateral views) displayed in Fig. 4-10. The spot splitting in the FFT pattern (Fig. 4-9b) indicates a certain degree of relaxation. Advanced analysis of this interface based on the mean separation between misfit dislocations have pointed out that (001)BZO nanodots are relaxed [153], as could be expected because of the high lattice mismatch. Formation of dislocations is a typical mechanism to relax the compressive strains of

heteroepitaxial growth of BZO thin films [214, 215], and have been observed in the present BZO dots.

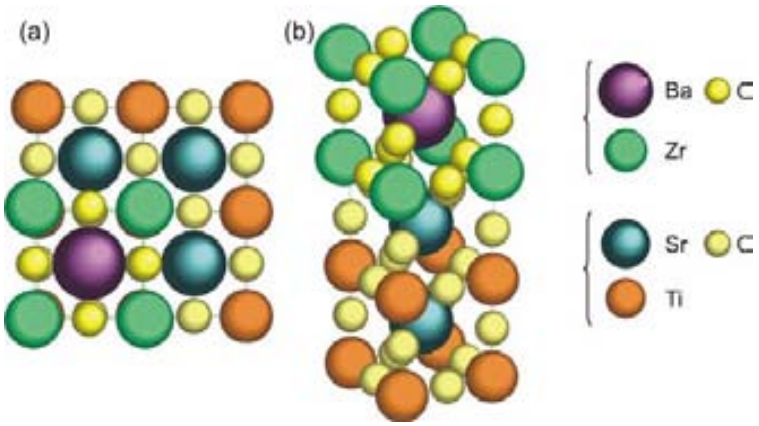

Fig. 4-10: Solid spheres model schematizing the cube-on-cube growth of (001)BZO on (001)STO: planar (a) and side (b) views.

Recalling AFM images in Fig. 4-8c, atomically flat terraces separated by one unit-cell steps of the (001)STO single-crystal can be clearly distinguished below (001)BZO nanodots. Terraces are about ~85 nm wide, which implies a miscut angle of ~0.26°. This value is in agreement with the step periodicities typically observed in our commercial single-crystal substrates once high temperature oxidizing treatments are performed (see also chapter 3). The observation of the bare substrate under BZO nanodots indicates that these nanostructures grow following a Volmer-Weber-like mechanism [23], as expected after the use of very dilute solutions and a system with high lattice mismatch. That is to say that due to the high interface energy, the strain energy of BZO/STO system is drastically reduced through the formation of 3D islands. We refer to a Volmer-Weber-like mechanism since islands' growth occurs from the amorphous layer formed after removal of organic material. On the other hand, Fig. 4-11 proves that nanodots nucleation occurs during heat treatment and it is not the result of inhomogeneous distributions of initial precursor solution, since a homogeneous amorphous layer is formed after deposition of ultradiluted solutions, i.e. 0.003 M.

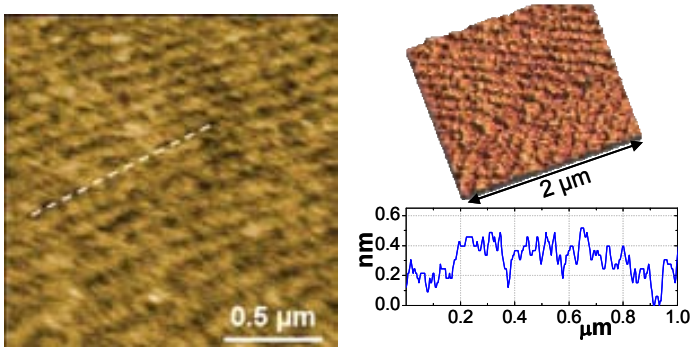

Fig. 4-11: Homogeneous coverage of (001)STO substrate is achieved after deposition of highly dilute BZO precursor solutions, i.e. 0.003 M, and prior to high temperature treatment.

Nanodots' separation along substrate terraces is observed to be much higher than the width of the terraces themselves, which indicates that diffusion is remarkably anisotropic. In general, 2D thin film growth on vicinal substrates is influenced by lattice steps through the so-called Ehrlich-Schwoebel barrier, which reduces atomic diffusion across steps with respect to diffusion within the terraces due to their modified chemical bonding at edges [58]. The extension of this barrier's influence on nanostructures' formation is complex since it depends on many microscopic details. Wide investigation has already been carried out in homo and heteroepitaxial growth on semiconducting and metallic surfaces within the context of nanowires formation [216, 217]; however, its role in oxide materials is still not well established.

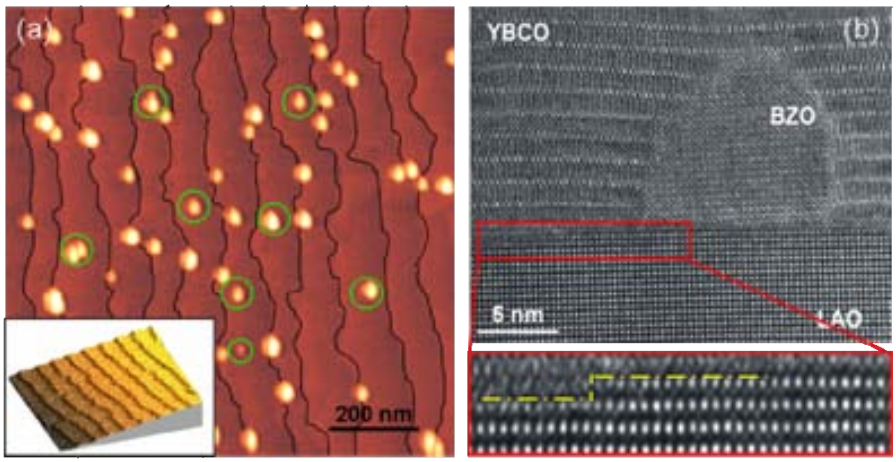

Fig. 4-12: Preferential localization of BZO nanodots at step edges of the substrate. In AFM image (a), the very few dots localized in the central part of the terraces are circled; additionally, substrate steps were brought out for a better visualization. The inset exhibits the morphology of the atomically flat terraces of a single-crystal substrate prior to deposition. TEM cross-section image (b) shows a (001)BZO nanodot placed at the upper side of a lattice step; a zoomed view of the step is displayed underneath. In this case, BZO-dot is surrounded by an $YBa_2Cu_3O_7$ thin film which was later deposited on top.

The observed BZO-nanodots distribution (Fig. 4-8c) suggests that an Ehrlich-Schwoebel barrier is also probably effective in the present oxide system for atomic diffusion perpendicular to lattice steps. It promotes the formation of BZO-dots within substrate terraces with heights much higher than lattice steps themselves (~15 times). As a result, it takes place an island step decoration phenomenon, where nanodots are preferentially located close to step edges instead of being placed in the centre of the terraces. From AFM topographic images, it is determined that the probability of a BZO nanodot to be placed next to step's edge, either in its up or bottom side, is ~4 times higher than to occupy the central part of the terrace. This preferential localization of BZO nanodots in relation to the substrate steps is emphasized in AFM image displayed in Fig. 4-12a, where the only dots situated in the centre of the terraces have been circled. The clean interface observed in TEM cross-section displayed in Fig. 4-12b enables to determine that the (001)BZO nanodot is located close to the upper side of a LAO lattice step; specifically, it is situated 5 nm from the step edge. In this TEM image, the BZO-

nanodot is surrounded by a superconductor $YBa_2Cu_3O_7$ (YBCO) thin film, which was later deposited on the nanostructured template. More details about the use of oxide nanostructured templates to improve superconducting properties of YBCO thin films are given in chapter 7.

The origin of this phenomenon (preferential localization of dots close to steps edge) is complex, as it essentially involves two main effects: bonding energy and relaxation of strain energy. Both energies contribute to the total energy of the system [218]

$$E = E_{surf} + E_{interface}(\kappa) + E_{relax}(\kappa^2,\varepsilon^2) \qquad \textbf{Eq. 4-4}$$

where κ refers to the curvature of the surface, E_{relax} is the elastic relaxation energy, E_{surf} is the surface energy per unit area and $E_{interface}$ is the interface energy related to the chemical bonding between atoms of the substrate's surface and the island ($E_{interface}$ is presented separated from E_{surf} to emphasize its dependence on κ). Competition between these two effects results in regions of local minima of energy which act as preferential nucleation centres. Atoms diffuse from regions of high energy to zones of lower energy, since atoms motion is governed by chemical potential $\mu \sim \partial E/\partial r$. This outcome has already been used to promote self-organization of semiconductor quantum dots in surfaces with induced relaxed strains achieved by lithographic techniques [218-221]. Mechanisms of assisted self-organization have been scarcely investigated in oxides till the moment; however, first assays performed in our group suggest an important potential for that methodology [222].

Hence, in the present system atoms are then expected to move from the central part of the terrace to step edge, as a mechanism to efficiently relax the energy of the system. Nonetheless, it must also be considered that strain in BZO nanodots is further relaxed through the formation of misfit dislocations, resulting in a semi-coherent heteroepitxay. This complex landscape might explain the preferential localization of BZO nanodots close to lattice step edges.

4.2.4.1 Influence of atmosphere, temperature and annealing time on monomodal populations of BZO nanodots

To investigate kinetic evolution of monomodal distributions of interfacial BZO nanodots, a study of the influence of growth parameters (atmosphere, temperature and annealing time) was also carried out for this particular solution concentration, i.e. 0.003M. Fig. 4-13 compares two equivalent BZO/STO templates (0.003M, 900^{o}C, 4h), one annealed in O_2 and the other in Ar-5%H_2. The monomodal distribution of BZO nanodots is maintained independently of the oxygen pressure in which they were processed. However, templates prepared in reducing atmosphere show higher density of BZO nanodots of smaller size and height than those prepared in O_2. The exact sizes of dots are difficult to determine within the lateral resolution limits of AFM, but a rough estimation leads to ~(21±8) nm in diameter and ~(7.5±2.1) nm in height for the nanodots' of sample annealed in Ar-H_2. These results agree with previous

examples carried out with more concentrated solutions (i.e. 0.03 M), where it has been shown that high oxygen pressure treatments enhance atomic mobility as compared to the ones processed in reducing atmosphere. Hence, it is confirmed that O_2 atmosphere promotes coarsening of BZO nanoislands resulting in lower density of larger dots.

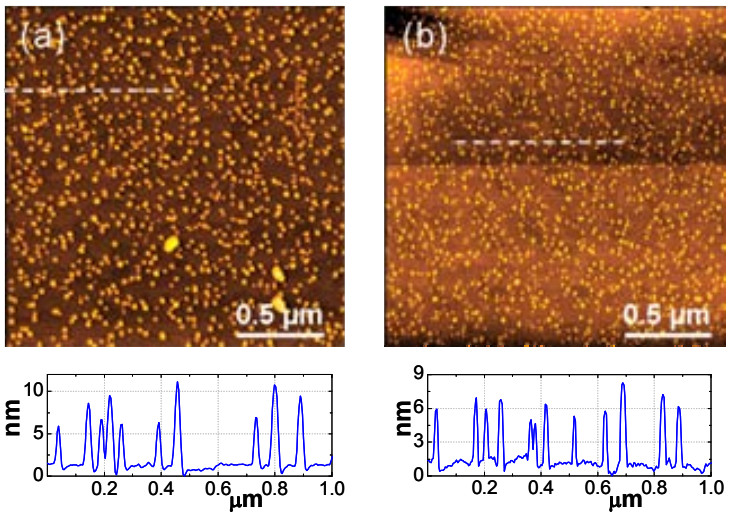

Fig. 4-13: AFM topographic images of BZO/STO templates prepared from 0.003M precursor solutions in oxidizing (a) and reducing atmosphere (b). In both cases, annealing was performed at 900°C for 4 h.

Less significant differences are observed between BZO interfacial nanodots prepared at distinct temperatures. Fig. 4-14 shows the AFM topographic images of two equivalent samples (0.003M, O_2, 4h), one annealed at 600°C (Fig. 4-14a) and the other at 900°C (Fig. 4-14b). Further XRD or TEM would be required to study possible differences in the degree of crystallization. However, the similarity of sizes within the AFM resolution limits indicates that once the first events have nucleated the interaction between them is very weak or of repulsive nature. It must be noticed that for these ultradiluted concentrations coarsening processes might occur through mechanisms distinct to that observed for higher concentrations (i.e. 0.03 M), where growth of nanoislands happens in part through material coming from the background.

Consequently, BZO nanodots grown from very dilute solutions are pretty stable, as it is evidenced through their slow mobility under different growth conditions. Thermodynamic analysis would be required to determine the equilibrium shape of (001)BZO nanoislands on STO substrates. These particular computations have not been carried out in the frame of this work. However, similar studies performed for the case of CeO_2 interfacial nanostructures have pointed out the possibility to generate monomodal distributions of stable nanodots with uniform shape and size and which do not undergo ripening phenomena; these thermodynamic analyses will be exposed in chapter 6.

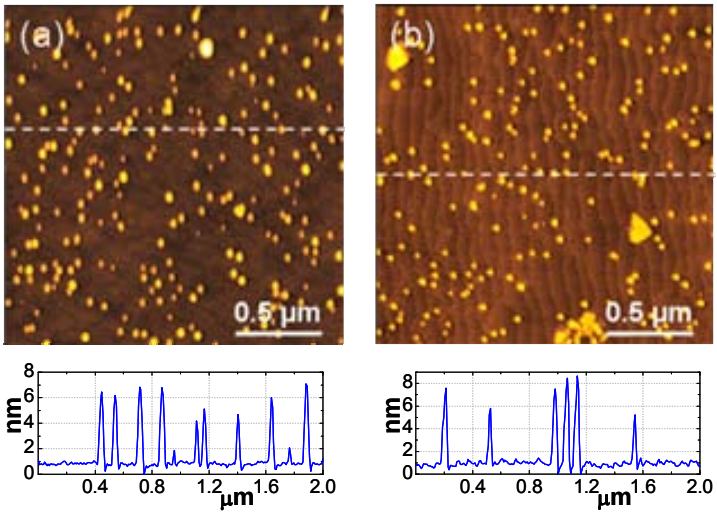

Fig. 4-14: BZO/STO templates prepared from 0.003 M precursor solution and annealed at 600°C (a) and 900°C (b) in high oxygen pressure for 4 h.

The presented systematic study about the influence of precursor solution and growth conditions on the formation of interfacial BZO nanostructures has served us as a model and general tool to explore the capabilities of CSD to prepare oxide nanostructured templates. Particularly, it has been proved that modification of growth conditions enables to tune the characteristics of the resulting interfacial nanostructures. This knowledge was used as a base for subsequent studies involving the generation of nanostructures of other interfacial oxide nanoislands.

4.3 Interfacial $Ce_{1-x}Gd_xO_{2-y}$ nanostructures

Ceria (CeO_2) is a fluorite oxide of significant relevance and interest in a wide range of areas, from hydrogen purification to coatings for superconductors, due to its intrinsic properties such as ionic conductivity or high dielectric constants [223-226]. Following the general trend of nanoscale materials, its performance and applicability is also expected to broader thanks to the capacity to generate structures at nanometric scale [76, 227]. Therefore, and taking into account that most of its technological applications are closely associated to its surface characteristics, it is of high interest to study the preparation of templates with interfacial CeO_2 nanostructures.

4.3.1 Interfacial CeO_2 nanostructures

After results obtained for BZO/STO system, and with the aim to generate templates with interfacial 3D CeO_2 nanostructures, it was worth to initially study the effect of solution concentration. Fig. 4-15 shows the AFM images of different samples prepared from precursor solutions with concentrations ranging from 0.1 M to 0.0025 M. All of them were annealed at 1000°C for 8 hours in oxidizing atmosphere. As substrates, previously high temperature

annealed $LaAlO_3$ (LAO) single-crystals were used. The system CeO_2/LAO has a lattice mismatch of ε~-1% for the epitaxial relation (001)CeO_2||(001)LAO provided that CeO_2 structure is rotated 45° with respect to [001] LAO axis.

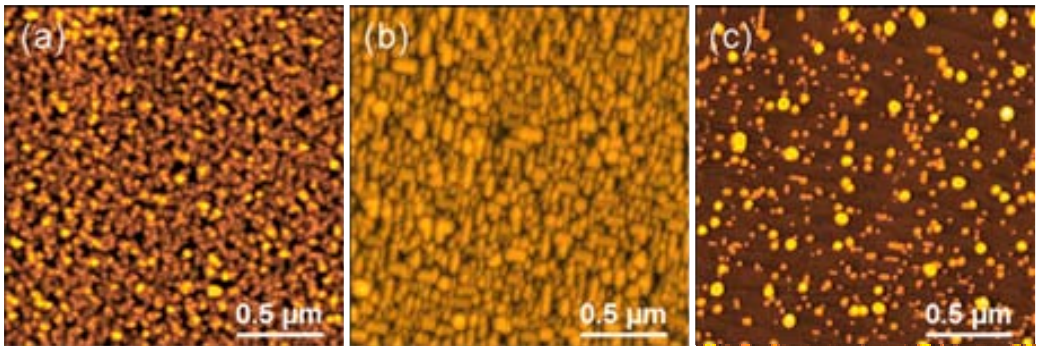

Fig. 4-15: CeO_2/LAO templates prepared from distinct precursor solution concentrations: 0.1 M (a), 0.025 M (b) and 0.0025 M (c). All them were annealed at 1000°C in oxidizing atmosphere for 8 hours.

For concentrations ranging from 0.1 M to 0.025M (Fig. 4-15a and b), there is nearly complete coverage of substrate. Sample's roughness (rms) decreases as precursor solution concentration is reduced, i.e. rms~ 5.9 nm for 0.1 M and rms~ 2.8 nm for 0.025 M. For concentrations about 0.0125 M and lower, the resulting templates exhibit isolated CeO_2 nanoislands, confirming that formation of 3D nanostructures is enhanced by using highly diluted solutions. Again, solution concentrations of ~10^{-3} M are the more promising ones for the generation of templates with monomodal size distributions of well-defined interfacial 3D nanoislands. Nanodots displayed in Fig. 4-15c were prepared from a 0.0025 M solution; they are (45 ± 10) nm and (6.7 ± 1.2) nm in equivalent diameter and height, respectively, and show a density of (89 ± 19) nanodots/µm^2.

4.3.1.1 Influence of atmosphere

As was showed for the case of BZO nanostructures, oxygen pressure plays an important role in the nucleation, growth and evolution of oxide nanostructures. Fig. 4-16 displays two CeO_2/LAO templates, one processed in O_2 (a) and the other in Ar-H_2 (b). Both samples were annealed at 1000°C, but while the former was treated during 8 h, the latter just remained 30 min in the furnace. Contrary to isomorphic CeO_2 nanodots obtained after oxidizing annealing, highly in-plane elongated nanostructures form in heat treatments carried out in reducing atmosphere. These anisotropic nanoislands (Fig. 4-16b) have fairly constant short axis width of ~(36±8) nm, but broad distribution of long axis lengths ranging from 100 nm to 700 nm. In general, longer islands are higher; though height's dispersion is just ~(16±7) nm. From the extraordinary length of nanostructures processed in Ar-H_2, and taking into account that this template was just submitted to 30 minutes treatment at 1000°C, it becomes evident that atomic

mobility in CeO_2 is drastically enhanced under these particular growth conditions (i.e. reducing atmosphere).

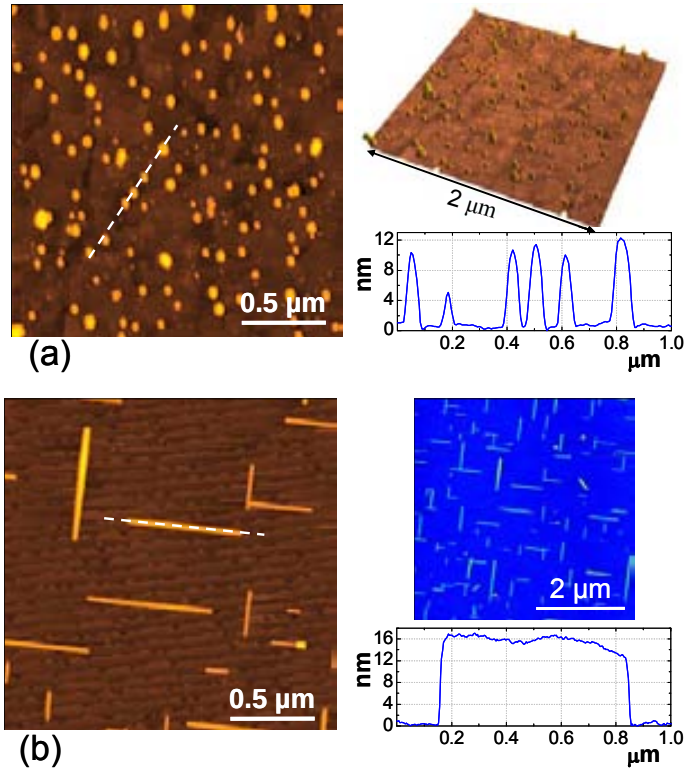

Fig. 4-16: CeO_2/LAO templates processed in distinct oxygen pressure, i.e. O_2 (a) and Ar-5%H_2 (b), at 1000°C during 8 h and 30 min, respectively. Distinct in-plane degree of anisotropy is observed: isomorphic structures form in oxidizing atmosphere, whereas highly elongate nanoislands grow in reducing atmosphere.

Improvement of atomic diffusion can be attributed to an increase of the number of oxygen vacancies in the fluorite structure, which facilitates atoms' jumps from their present site to a neighbour one. Both samples were annealed at 1000°C, thus growth temperature is not the cause of the observed differences (section 4.2.2). Instead, the particular chemistry of CeO_2 could be the responsible. Ceria Ce^{4+} can reduce itself to Ce^{3+} and, as a result, an oxygen vacancy is created by charge compensation. It has been reported that for a partial oxygen pressure $P(O_2)$=1 bar the ratio between oxygen atoms and Ce ones is O/Ce~2; nevertheless, ratio O/Ce decreases to 1.87 if oxygen partial pressure is reduced to 10^{-15} bar [223]. Therefore, in the present case, the observed increase in CeO_2 mobility is associated to the use of a reducing atmosphere, which promotes oxygen vacancies formation due to Ce reduction.

Pushed by this behaviour, and with the aim to study nucleation processes and further evolution of the system, it became straightforward to look for the more efficient path to introduce oxygen vacancies in CeO_2 structure in order to enhance atomic mobility. This approach is presented in the next section.

4.3.2 Interfacial $Ce_{1-x}Gd_xO_{1-y}$ nanostructures

4.3.2.1 Effect of Gd-doping in CeO_2 structure

In addition to oxygen vacancies formation through oxygen partial pressure regulation, an alternative or additional strategy consists of doping CeO_2 lattice with lower valence metal oxides, such as Sr^{2+}or Gd^{3+} [228, 229]. The added dopant agent occupies a Ce^{4+} site of the host lattice and, as a result, an oxygen vacancy is created to compensate electrical charge. Hence, combination of reducing atmosphere plus aliovalent doping seemed to be the finest approach to enhance CeO_2 mobility.

To select the optimal dopant agent, a trivalent cation with electronegativity similar to that of ceria is preferred. Thus, rare-earth elements are the best choice [230]. Furthermore, it is desired a dopant agent of a size close to that of ceria in order to preserve the fluorite lattice [223]. When taking into account all these considerations, Gd arises as an excellent candidate for CeO_2 doping.

Compatibility between Gd doping and MOD process in $Ce_{1-x}Gd_xO_{2-y}$ (CGO) thin films growth has already been investigated in our group by Coll *et all*. [97, 184]. Results indicated that best performance in terms of CGO epitaxial thin films growth was achieved in Ar-H_2 for a concentration of 10% of Gd-doping (which is the concentration showing highest ionic conductivity). Gravimetrical measures [231] have shown that at $P(O_2)=10^{-15}$ bar, the ratio O/M (where M=metals, i.e. M=Ce+Gd) is ~1.87 for CGO and ~1.85 for CeO2, and at $P(O_2)=1$ bar this ratio can be reduced from form O/M~2 to ~1.95 if CeO_2 fluorite structure is doped with 10%-Gd. Hence, the concentration of vacancies is significantly improved merely through doping. Consequently, within the frame of this work we will just focus on the generation of interfacial $Ce_{0.9}Gd_{0.1}O_{2-y}$ nanostructures. So, from now on, the acronym CGO will stand for the particular dopant concentration of 10%-Gd. Particularities of solution preparation are indicated in chapter 3.

4.3.2.2 Influence of solution concentration on interfacial $Ce_{0.9}Gd_{0.1}O_{2-y}$ (CGO) nanostructures

Taking advantage of this knowledge about Gd-doping [97, 184] and previous studies performed in BZO/STO and CeO_2/LAO systems, a brief scan of the influence of precursor solution concentration on the formation of CGO nanostructures was initially carried out. Concentrations ranging from 0.25 M to 0.002 M were studied. Growth was performed at 1000ºC in Ar-H_2, for just 30 minutes in the more diluted cases and 8 h for the most concentrate solution (0.25 M), since longer annealings are required to ensure complete crystallinization of

thicker layers. Corresponding AFM images are displayed in Fig. 4-17. As substrates, LAO single-crystals heat treated in O_2 were used.

Under these growth conditions, the network of parallelepiped structures of orthogonal crystallites that characterizes CeO_2 thin films is preserved as solution concentration is reduced. Since the total amount of deposited material diminishes, island's density also decreases finally resulting into the formation of isolated nanostructures for very dilute solutions. A thin film of about ~20 nm thick and roughness rms~12 nm is typically obtained from 0.25 M precursor solutions (Fig. 4-17a). Decreasing solution's concentration, the formation of isolated elongated 3D nanostructures is effectively promoted. Consequently, nanostructured templates with highly in-plane anisotropic interfacial 3D nanostructures are obtained for concentrations ranging from 0.01 M to 0.005 M, two examples are displayed in Fig. 4-17b and c.

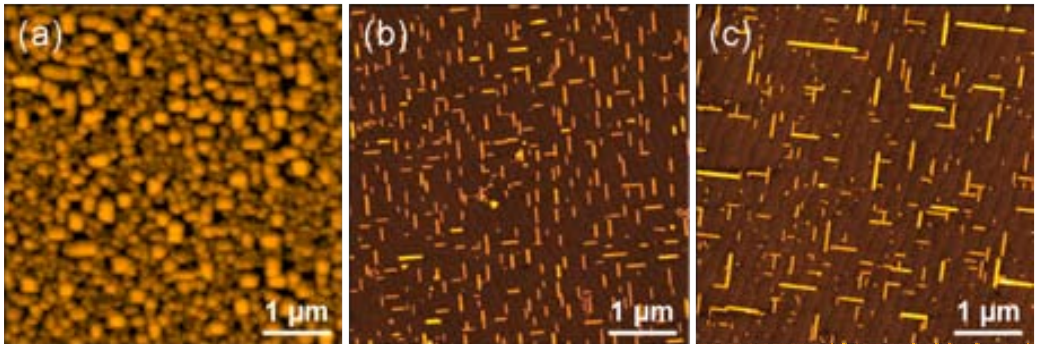

Fig. 4-17: CGO/LAO templates prepared from distinct precursor solution concentrations: 0.25 M (a), 0.01 M (b) and 0.008 M (c). All samples were processed at 1000ºC in reducing atmosphere for 30 min; just thicker sample of 0.25M (a) was annealed for 8 h.

CGO/LAO template shown in Fig. 4-17b was prepared from 0.01 M precursor solution. Interfacial CGO nanoislands' short *a* and long *b* axis measures (39±7) nm and (172±55) nm, respectively. They are ~7.6 nm high, and a medium density of ~16 islands/µm^2 is computed in distinct regions of the sample. Formation of elongated nanoislands is as well appreciated in template displayed in Fig. 4-17c, which was prepared from 0.008 M precursor solution. These islands are ~8 nm in height and there is a mean density of ~11 nanowires/µm^2. All them keep their axis' width around ~(36±10) nm (within AFM resolution limits), though their long axis lengths can range from 102 to 1040 nm. For easiness of calculations carried out in chapter 6 and for consistency through the whole work, we will define lateral aspect ratio as $c=(b/a)^{½}$. Accordingly, nanoislands displayed in Fig. 4-17c exhibit lateral aspect ratios as large as $c=(b/a)^{½}$~5.4, which means that one wires' axis is 29.2 times larger than the other. On the other hand, due to these high lateral aspect ratios, we tend to refer to these elongated nanostructures as *nanowires*. Hence, in general, nanowires show narrow distribution of short axis widths, whereas there is a broad dispersion of lengths, which results in these extraordinary anisotropic lateral aspect ratios. CGO elongated nanostructures are nearly exclusively aligned along the

crystallographic substrate soft axis [100] and [010]; so, there exist two families of nanowires orthogonally in-plane oriented. As a result, templates with self-organized nanostructures are achieved. A high tendency of nanowires to interact between each other along these directions of the substrate is often appreciated (see Fig. 4-17c), resulting into dimers and trimers of nanoislands, and even more intricate nanostructures. In template displayed in Fig. 4-17c, in addition to nanowires, there also exist some smaller nanoislands of ~(34±7) nm in equivalent diameter and ~6.4 nm high. From AFM images it cannot be established whether they exhibit a low degree of anisotropy or, contrary, they are isomorphic nanostructures. For templates prepared from solutions of 0.004 M, nanowires are still formed but their density is of just 0.04 wires/μm^2 due to the ultradiluted solutions used. For lower concentrations, i.e. 0.002 M, just isolated nanoislands of ~(77±25) nm equivalent diameter and density (0.21±0.01) islands/μm^2 are observed, the degree of anisotropy of these nanostructures can neither be determined from AFM images.

Under nanowires, the atomically flat terraces separated by one unit-cell high steps of the substrate are visible in templates shown in Fig. 4-17b and c, indicative that a Volmer-Weber-like growth mechanism was followed. For very small nanowires' sizes, it is detected a slight tendency of wires to remain within terrace boundaries. However, once their length exceeds terraces' width, no correlation between positioning of elongated nanoislands and substrate steps is observed. Instead, nanowires seem to easily cross them, elongating along [100] and [010] substrate directions.

In general, the mean distance that separates CGO-nanowires in Fig. 4-17b and c is about 250-300 nm, which is larger than the typical separation ~100-150 nm observed between BZO or CeO_2 nanodots. When also taking into account that just 30 minutes of heat treatment were required for the formation of these extremely long CGO nanostructures (in front of the 4-8 hours typically used for BZO/STO and CeO_2/LAO systems), it becomes evident that we are dealing with a system (CGO/LAO) which displays an ultrafast kinetics under these particular growth conditions, i.e. high temperature and reducing atmosphere. Let's notice that similar elongated nanostructures were also observed in CeO_2/LAO system when processed in Ar-H_2 (Fig. 4-16b). This resemblance suggests that the number of vacancies created by Gd-doping is largely exceeded by the quantity created simply using a reducing atmosphere. These results are in agreement with gravimetrical measurements [231], where an oxygen to metal ratio O/M~1.87 was determined for CeO_{2-y} and O/M~1.85 for $Ce_{0.9}Gd_{0.1}O_{2-y}$ at $P(O_2)=10^{-15}$ bar, being M the total metals present in the system (i.e., M=Ce +Gd for CGO).

4.3.2.3 Influence of atmosphere on CGO nanostructures

The studies exposed above about the influence of precursor solution concentration on the formation of CGO nanostructures were carried out in Ar-H_2. This reducing atmosphere was initially chosen because it was the one providing a highest epitaxial fraction in CSD-CGO thin films, as a result of a highly enhanced mobility [97, 184]. The particular role of Gd-doping in the formation of CeO_2 nanostructures can be studied in high oxygen pressure annealings, where oxygen vacancies formation trough Ce^{4+} substitution by Gd^{3+} might be counteract by the oxidizing atmosphere, which pushes against oxygen vacancies formation.

With that purpose, two equivalent samples (0.008 M, 1000ºC, 30 min) were grown under different oxidizing/reducing pressures. Fig. 4-18 shows the corresponding AFM images. Sample illustrated in Fig. 4-18a was processed in Ar-5%H_2, whereas for sample displayed in Fig. 4-18b the growth was carried out at 1 bar of O_2. The morphological differences between both templates are notable. The former corresponds to the already described case of highly in-plane anisotropic CGO nanowires, divided in two families in-plane orthogonally distributed. The latter (Fig. 4-18b) shows a high density (~510 dots/μm^2) of isomorphic nanodots of (19±9) nm in equivalent diameter and ~2.1 nm in height, which are localized in rows resulting in highly ordered templates. Within AFM resolution limits, these nanodots clearly resemble CeO_2 isomorphic nanostructures formed in oxidizing atmosphere (Fig. 4-16a), though in the present case nanodots are smaller because they were just submitted to 30 min annealing instead of 8 h.

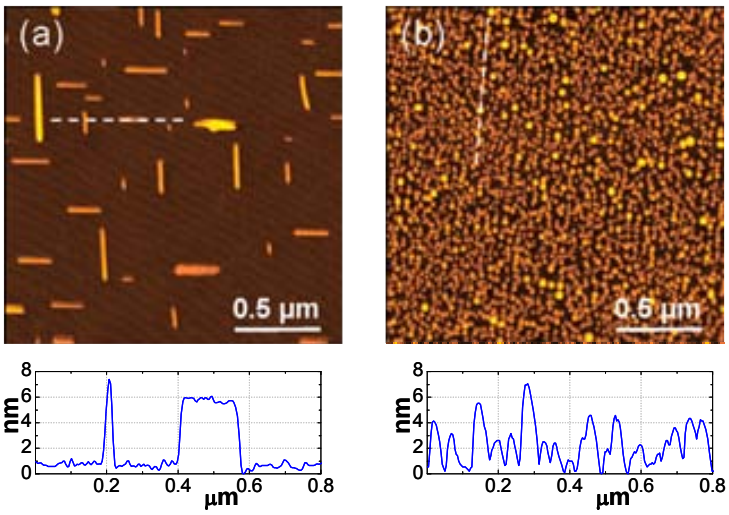

Fig. 4-18: CGO/LAO templates annealed in Ar-H_2 (a) and O_2 (b) atmosphere, respectively. Both of them were prepared from 0.008 M precursor solution, and treated 30 min at 1000ºC.

4.3.2.4 Influence of growth temperature on CGO nanostructures

As observed beforehand in BZO and CeO_2 nanostructures, temperature is another key parameter to investigate when studying the mobility of the system (Eq. 4-3). Fig. 4-19 shows

the AFM images corresponding to equivalent CGO/LAO templates grown at 600ºC (a), 800ºC (b) and 1000ºC (c). All them were prepared from 0.008M precursor solution and annealed 30 min in Ar-H_2, which was observed to be the atmosphere providing highest mobility in CGO.

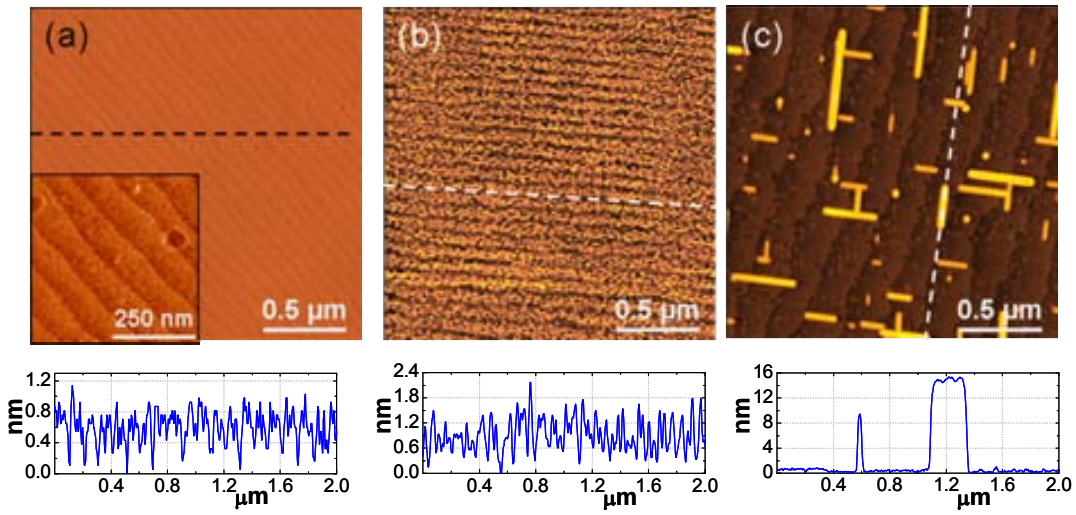

Fig. 4-19: CGO/LAO templates annealed at 600ºC (a), 800ºC (b) and 1000ºC (c) during 30 min in reducing atmosphere. A precursor solution of 0.008M was used in all cases.

After 30 min of heat treatment, samples grown at lower temperature (600ºC_Fig. 4-19a) show an amorphous layer covering all the substrate with an average roughness ~ 0.21 nm; any well-defined 3D island is observed. At 800ºC (Fig. 4-19b), the roughness of the template increases up to rms~ 0.39 nm, suggesting a slight tendency towards the growth of 3D islands. Nevertheless, longer annealing times are required for their formation, as it will be studied in detail in next chapter 5. At 1000ºC (Fig. 4-19c), the previously reported highly elongated nanowires form. Hence, temperature is also a critical parameter determining the ultrafast kinetics experienced by interfacial Gd-doped CeO_2 nanostructures in reducing atmosphere.

The distinct atomic diffusion reflected by the stage of evolution and definition of the resulting interfacial CGO nanostructures is associated to the dependence of the number of vacancies with temperature. At $P(O_2)=10^{-15}$ bar and 700ºC the oxygen deficiency x in $Ce_{0.9}Gd_{0.1}O_{1.95-x}$ is less than 10^{-3}, whereas at 1000ºC it has increased up to 0.1 [231]. Therefore, as higher is the temperature, higher is the concentration of vacancies in the fluorite structure and higher the atomic mobility of the system.

From all examples above, it is derived that we are dealing with a very singular system, CGO/LAO. Highly distinct interfacial 3D nanostructures form depending on particular processing conditions. Isomorphic or anisotropic nanoislands, ordered into rows or located orthogonally along substrate soft axis, with lateral sizes within the range of tens or hundreds of nanometers, present with ultrahigh or ultralow densities, etc. are examples of the contrasted

singularities of the two sorts of interfacial CGO nanoislands grown. Therefore, fine selection of growth conditions is as a powerful tool to tune and control islands' characteristics (morphology, distribution, size, density). Oxygen pressure, temperature and time of heat treatment are proved to play a crucial role in the formation and evolution of distinct kind of nanostructures. The concentration of oxygen vacancies created in CGO structure in O_2 and Ar-H_2 plays as well an important role in the formation of the resulting nanostructures. Nonetheless, there could be other arguments, i.e. thermodynamic, that could make the distinction. So, CGO arises as a highly interesting model system to study thermodynamics and kinetic mechanisms on chemically-derived strain-induced oxide nanoislands. Therefore, next chapters 5 and 6 will be entirely deserved to exhaustively study interfacial CGO nanostructures from nucleation to advanced evolution stages, from self-assembled to self-organized processes, from an experimental to theoretical point of view.

4.3.3 Crystallographic orientation of CGO thin films

Despite detailed studies will be carried out in next chapters, first tracks about the origin of the amazing differences observed between distinct CGO nanostructures can be extracted from CGO thin films grown on LAO single-crystals substrates. The growth of fluorite structures on substrates with also fluorite structure has been widely studied [181, 232]. However, the dissimilar growth of fluorite on perovskite substrates has been scarcely investigated [159, 192, 233]. Particularly, to our knowledge there is not any study based on the deposition of chemical solutions. Therefore, in addition to the generation of interfacial nanostructures, we ran in parallel a study of the influence of growth conditions on CGO thin films grown on LAO single-crystals by CSD. These investigations gave us the first clues about some of the differences between CGO nanostructures.

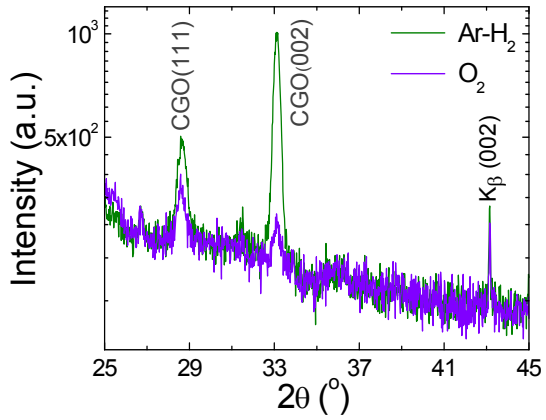

Fig. 4-20: XRD θ-2θ scans of two CGO thin films grown on LAO single-crystals from 0.25 M precursor solution and processed 8 h at 1000°C in reducing (—) and oxidizing (—) atmosphere.

Studies presented above (section 4.3.2.3) pointed out the important role of oxygen pressure in the morphology of the resulting interfacial CGO nanoislands. In view of that, Fig. 4-20 shows XRD θ-2θ scans of CGO/LAO thin films prepared from 0.25 M solution and processed 8 h at 1000°C in Ar-H_2 reducing and O_2 oxidizing atmosphere, respectively. The peaks observed correspond to reflections (002) and (111) of CGO. The intensity of these reflections is higher for the film grown in Ar-H_2, indicative of a higher volume of epitaxy in the films processed under these conditions. Thus, it confirms that reducing atmosphere promotes the generation of higher concentration of oxygen vacancies, which leads to a enhanced atomic mobility and, consequently, it allows to faster develop epitaxy in the system. Moreover, it is also remarkable to observe that the relative fraction of intensities between both reflections, Q=I(111)/[I(111)+I(002)], is distinct, i.e. Q_{O2}=0.56 and Q_{ArH2}=0.33. Hence, the nucleation of distinct crystallographic orientations seems to depend on the atmosphere.

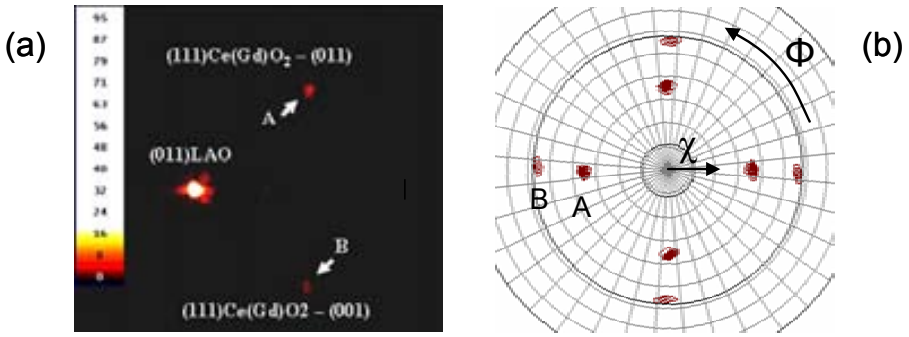

Fig. 4-21: XRD² pattern (a) showing the reflections (111)-CGO and (011)-LAO of a CGO/LAO thin film grown at 1000°C in Ar-H_2 atmosphere. Pole figure of the same film corresponding to (111)-CGO (b), where peaks observed at χ=35° and χ=54° correspond to CGO domains oriented (011) (A) and (001) (B), respectively.

Crystallographic information of just planes lying parallel to substrate is obtained from conventional XRD measurements. To obtain further information, (111)-CGO pole figure was investigated through X-ray measurements using a bidimensional detector (XRD²). The advantage of XRD² bases on the possibility to simultaneously measure a large range of 2θ-χ values (see also chapter 2). Fig. 4-21 displays the XRD² measurements of a CGO/LAO thin film annealed in Ar-H_2. Specifically, Fig. 4-21a shows a 2θ-χ frame, whereas Fig. 4-21b exhibits the ϕ-scan of (111)-CGO constructed from a set of frames taken at distinct ϕ values. Surprisingly, and complementary to expected results, the intensity corresponding to (111)CGO grains is negligible. Thus, this phase represents a very minute volume of the total layer; and if it was detected in XRD measurements was just because it is the reflection of highest intensity. The observed reflections of (111)-CGO (Fig. 4-21a) at χ=54° (B) and χ=35° (A) correspond to CGO crystallographic orientations (001) and, unexpectedly, to (011), respectively. Due to the designed configuration of measurement, and because we worked with a 2D-detector, the reflection (011) of (001)LAO substrate was also observed in the same frame. The integration of

(111)-CGO peaks in Fig. 4-21a corresponding to domains (001) and (011) reveals that domains oriented (011) represent 79% of the volume of the film treated in reducing atmosphere, whereas the rest basically corresponds to domains (001). Therefore, the dominant crystallographic orientation of CGO/LAO thin films grown in Ar-H_2 is the (011), which was not detected by XRD because it overlaps with (002) peak of LAO. These distinct crystallographic orientations and ration of intensities will be a key factor to explain the formation of either dots or wires depending on oxygen pressure during annealing.

Temperature was also found to be a critical parameter for the formation of interfacial CGO nanostructures (section 4.3.2.4). An idea of the influence of temperature on CGO thin films is given in Fig. 4-22. It displays XRD θ-2θ scans of CGO/LAO thin films processed 8 hours in reducing atmosphere at distinct temperatures; 0.25 M precursor solution was used. In agreement with results in Fig. 4-20, (111) and (001) reflections of CGO were detected by conventional XRD measurements. The intensity of these Bragg reflections (Fig. 4-22a) increase as higher is the annealing temperature. Thus, the epitaxial volume of CGO thin film also increases with temperature, since atomic mobility is also function of temperature (Eq. 4-3). Fig. 4-22b shows the evolution with temperature of the relative fraction Q=I(111)/[I(111)+I(002)] of (002)-CGO orientation with respect to (111). These analysis indicate that the proportion of CGO film oriented (111) reduces as temperature raises. For 1000ºC and higher annealing temperatures, the ratio between both orientations is kept fairly constant despite layer epitaxy continues to increase.

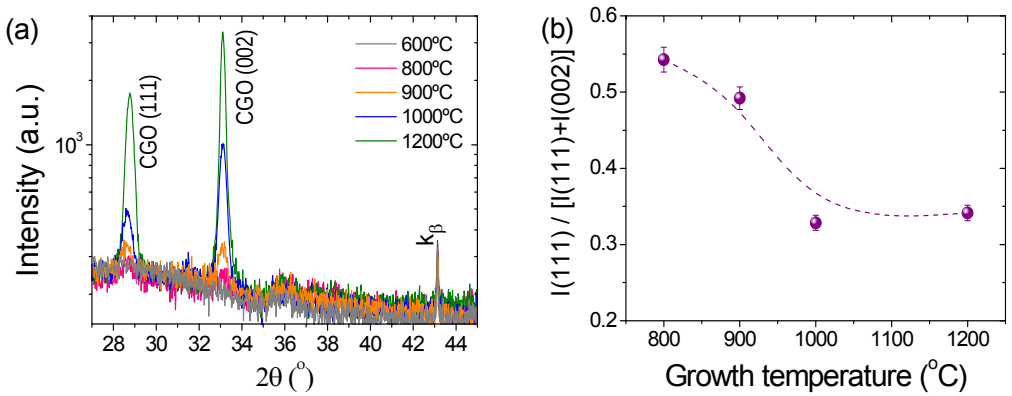

Fig. 4-22: Crystallographic orientation of CGO thin films grown on LAO substrates by CSD: XRD 2θ-scans showing the evolution of the (111) and (002)-CGO reflections as function of the annealing temperature (a). Intensity of the (111) orientation normalized with respect to the sum of the (111) and (002) intensities is also plotted as function of temperature (b). All samples were prepared from 0.25 M solutions and processed 8 h in reducing atmosphere.

All these results based on thin films suggest that the growth of the fluorite CGO on substrates with different crystallographic structure must be very sensible to growth conditions, i.e. nucleation of CGO on LAO is modified through temperature and oxygen pressure. This

behaviour seems to be clearly reflected in the resulting interfacial nanostructures, as will be deeply analyzed in chapter 5.

4.4 Interfacial La_2O_3 nanostructures

The systematic and extended studies on BZO/STO and CGO/LAO systems have proved the versatility of CSD for the generation of interfacial self-assembled oxide nanoislands. Combination of similar and dissimilar structures (perovskite-perovskite, fluorite-perovskite) as well as tuning of growth conditions has proved to allow the generation of large variety of interfacial nanostructures with distinct shapes, sizes and densities. Thus, the present subsection just pretends to be an overview over another combination of structures, La_2O_3/LAO, to have one more example about the capabilities of the methodology presented.

Like most of rare-earth oxides, lanthana has good mechanical, thermal, chemical, optical, etc. properties [234-236], which makes it very attractive for applications. For example, it arises as an excellent candidate for next generation of high κ gate insulator applications due its high dielectric constants [235, 237]; other potential applications are in catalysis [238] or optics [239]. La_2O_3 can adopt two distinct crystallographic structures, i.e. cubic and hexagonal mainly depending on processing temperature [240], which are expected to be reflected on the resulting interfacial nanoislands. Nonetheless, it is known that La_2O_3 is chemically unstable in ambient air.

4.4.1 Influence of growth temperature on interfacial La_2O_3 nanostructures

Previous studies point to precursor solutions within the range of 0.01M-0.003M as the optimum concentrations for the generation of interfacial oxide nanostructures by CSD. Therefore, for the present preliminary studies on La_2O_3 we just restricted to that concentration range. Details on the preparation of the solutions are reported in chapter 3. Thermally treated in O_2 LAO single-crystals were used as substrates.

Fig. 4-23 shows AFM topographic images of La_2O_3/LAO templates processed at distinct temperatures: 700^{o}C (a), 800^{o}C (b) and 1000^{o}C (c). All them were prepared from 0.008M precursor solution and annealed 30 min at 1 bar oxygen pressure at the corresponding temperature. At 700^{o}C (Fig. 4-23a), most of deposited material is homogeneously covering the substrate as an amorphous layer of roughness rms ~ 0.25 nm. The first crystallographic nuclei start to emerge from the amorphous background. These nanoislands are grouped in clusters of mean diameter ~450 nm, and the mean height of the islands constituting them is about 2-4 nm, as appreciated in the corresponding profile.

Templates processed at 800°C (Fig. 4-23b) exhibit well-defined 3D rectangular islands with top flat surfaces. The height of these islands is (6.5±1.3) nm, and their mean diameter $D=(ab)^{½}$ is (850±150) nm. Despite being mostly anisotropic, the largest lateral aspect ratio $c=(b/a)^{½}$ observed does not exceed ~1.6 (i.e. one side 2.5 times larger than the other). The large D size of these islands and their in-plane aspect ratio results into a morphology distinct from all previous examples, which is essentially characterized by the extremely flat large area surfaces at islands' top. Additionally, few higher islands with smaller lateral sizes are also observed in these templates. Their shape and size resemble La_2O_3 nanoislands grown at higher temperature; thus, they are described in next paragraph.

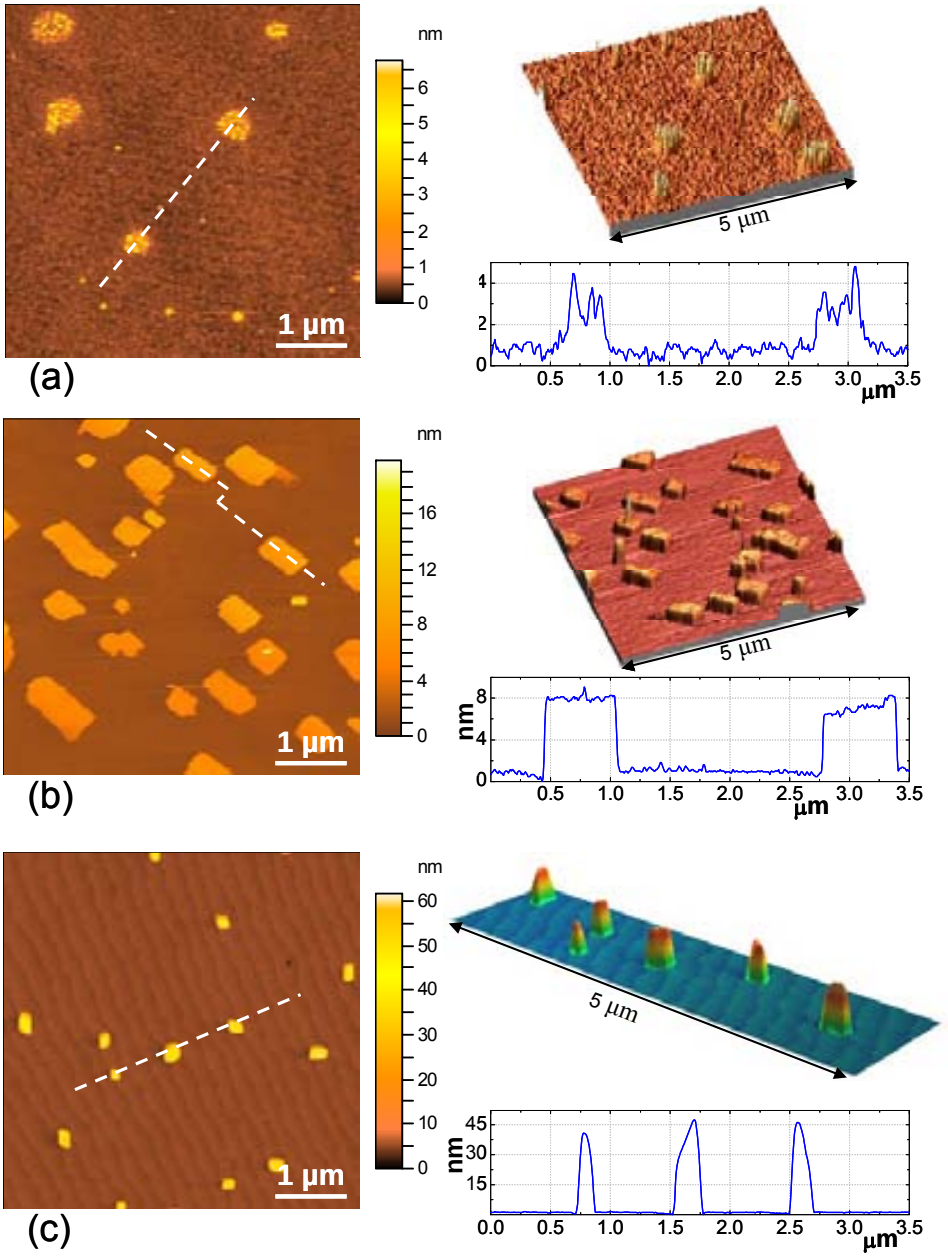

Fig. 4-23: La_2O_3/LAO templates processed at temperatures: 700°C (a), 800°C (b) and 1000°C (c). All them were prepared from 0.008M precursor solution and annealed 30 min at 1 bar oxygen pressure at the corresponding temperature.

At 1000ºC (Fig. 4-23c), the resulting 3D interfacial La_2O_3 nanoislands are dome-shaped with average diameter D~(218±18) nm and height h~(46±9) nm. These dimensions results in height-to-lateral aspect ratios h/D ~0.21; values ~28 times higher than those observed in flat La_2O_3 islands processed at 800ºC. This z-axis grow might be associated to the high interfacial energy of La_2O_3/LAO (Table 4-1), which promotes height growth instead of lateral extension. At this temperature (1000ºC), similar interfacial nanoislands were also obtained in templates treated in reducing atmosphere. Thus, the strong dependence of atomic mobility on oxygen pressure typically observed in previous example systems (BZO/STO, CGO/LAO) does not apply to the present case.

Summary of the height and equivalent diameter of interfacial La_2O_3 nanostructures as function of growth temperature is displayed in Fig. 4-24a. In addition to commented templates, results corresponding to other annealing temperatures have been included, confirming the described tendencies. All samples were also prepared from 0.008M and annealed 30 min in O_2. Fig. 4-24b exhibits the extraordinary evolution of height-to-diameter ratio as function of growth temperature of these nanoislands.

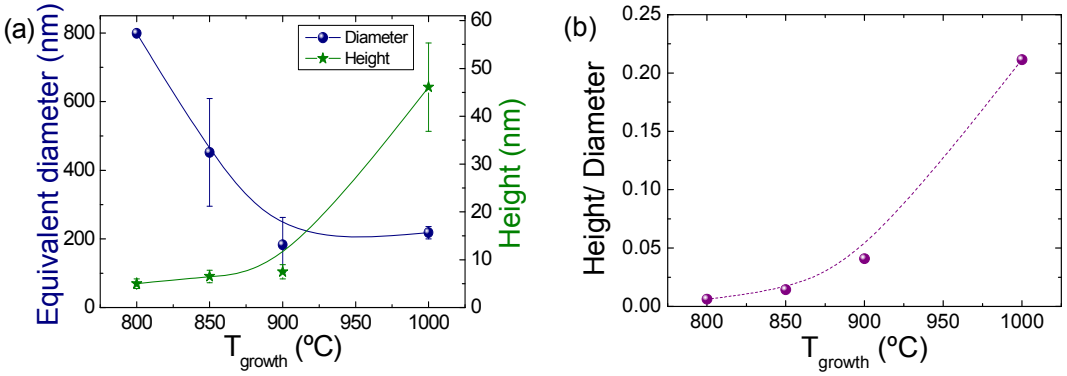

Fig. 4-24: Equivalent diameter and height (a) of La_2O_3 nanoislands as function of heat treatment temperature; the corresponding evolution of height/diameter ratio is also plotted (b). All templates were prepared from 0.008M precursor solution and annealed 30 min in O_2 at the corresponding temperature.

TEM images displayed in Fig. 4-25 and Fig. 4-26 correspond to a La_2O_3/LAO template processed at 825ºC for 30 min in air; thus, the two distinct island's morphologies previously described are distinguished. Flat-terminated islands (Fig. 4-25) are identified with the monoclinic phase lanthanum oxide hydroxide (LaO(OH)); FFT points out the epitaxial relationship with the substrate is (001)La_2O_3[110]||(001)LAO[100]. This phase might derive from the cubic La_2O_3 structure, which has been observed to rapidly transform into LaO(OH) after the absorption of water from the air [240]. However, more studies are required to discard that this phase does not already form during heat treatment because of the water remaining in the atmosphere.

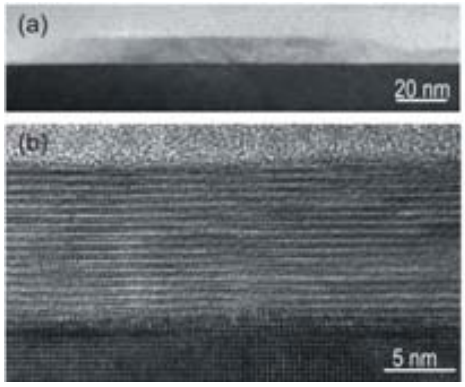

Fig. 4-25: Low (a) and high (b) magnification high-resolution TEM cross-section images of a monoclinic LaOOH nanoisland on a LAO substrate.

Fig. 4-26 shows several TEM images of large dome-shaped nanoislands; high resolution images and FFT reveal that they have crystallized in a mixture of hexagonal phases. In some regions these islands have crystallized as hexagonal La_2O_3 with the epitaxial relationship (100)La_2O_3[001]||(001)LAO[100], whereas other regions have crystallized as hexagonal lanthanum oxide carbonate ($La_2O_2CO_3$). Longer annealing times are needed to determine if the presence of carbon is a residue of the amorphous film or consequence of post-annealing reaction with CO_2 in the air. Notice that regions corresponding to hexagonal La_2O_3 phase show well-defined facets; in contrast, zones corresponding to $La_2O_2CO_3$ are round-shaped.

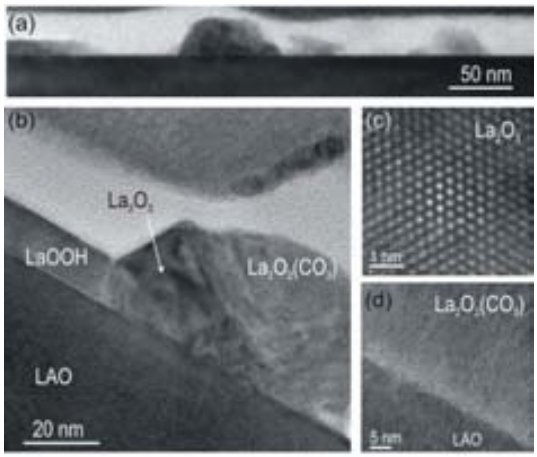

Fig. 4-26: TEM cross-section images of dome-shaped nanoislands corresponding to a mixture of hexagonal phases La_2O_3 and $La_2O_2CO_3$: low (a) and high (b) magnification images, details of the hexagonal La_2O_3 (c) and $La_2O_2CO_3$ (d) lattices.

4.4.2 Evolution of La_2O_3 nanostructures

Fig. 4-27 shows the evolution of La_2O_3 interfacial nanoislands on LAO substrates at a given temperature, i.e. 850^{o}C. The studied template was prepared from 0.01M precursor

solution and heat treated in oxidizing atmosphere. Dimensions of islands as function of annealing time are displayed in Fig. 4-28.

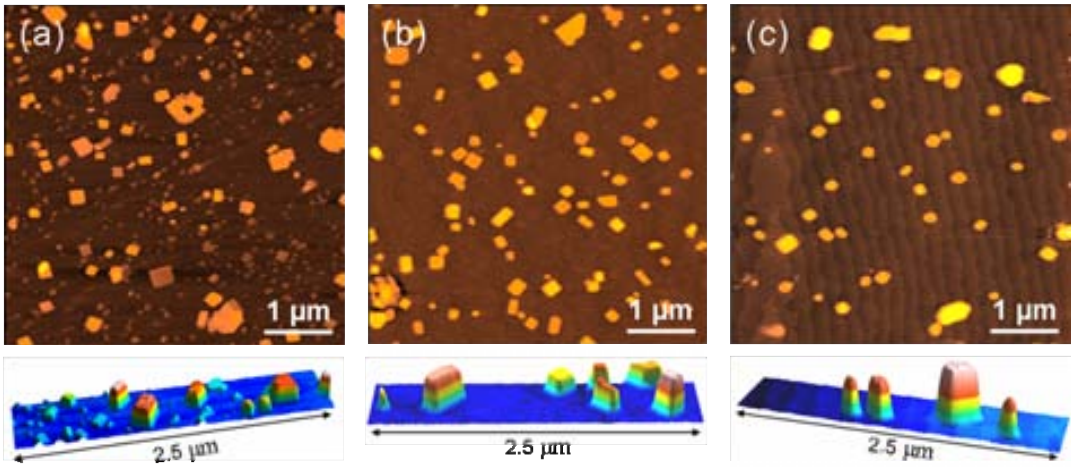

Fig. 4-27: Evolution of La_2O_3 nanoislands on LAO substrates at 850°C in oxidizing atmosphere. The AFM images correspond to snapshots taken after heat treatments of 30 min (a), 1 h (b) and 3 h 30 min (c). The same proportional relation between the height of islands in 3D profiles and their real height has been used for all distinct evolution stages. The sample was prepared from 0.01M solution.

As anneal proceeds, the size and height of the islands continuously increases at the same time that their density decreases. This coalescence behaviour stands till annealing times of ~1 hour (i.e. from Fig. 4-27a to b). For longer heat treatments, islands' height continues to increase, though their size is kept fairly constant at D~200 nm. Meanwhile, the density of islands slowly diminishes. Thus, this second coalescence phenomena driving the evolution of the system (exemplified between Fig. 4-27b and c) is distinct from that observed at first evolution stages. The mechanism leading this path might be associated with strain and interface energy. In heteroepitaxial growth, islands' formation is the more efficient route to reduce strain energy due to lattice misfit between structures. For a high lattice mismatched system, as we know to be the

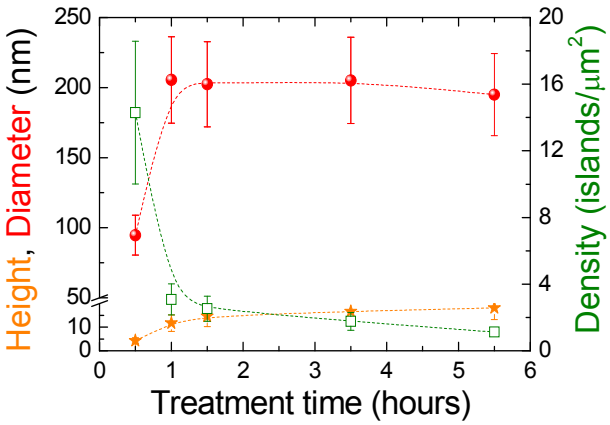

Fig. 4-28: Height (▲_left axis), diameter (●_left axis) and density (□_right axis) of La_2O_3 nanoislands on LAO substrates as function of heat treatment time. Anneal was done at 850°C in oxidizing atmosphere; the precursor solution was 0.01M.

case after TEM analyses and Table 4-1, growth upwards is a priori more favoured than lateral extension, if no other relaxation mechanisms are present [29], since vertical growth direction allows the relaxation of highest planes of the island towards its intrinsic lattice parameter.

The increase of islands' height as annealing proceeds is clearly illustrated in Fig. 4-29. The same proportional relation between 3D profile height and real height of La-based nanostructures has been applied to the different evolution stages. These particular 3D profiles correspond to heat treatments at 850ºC of 30 min, 1 h and 3 h 30 min; despite belonging to the same sample, they do not correspond to the same group of islands.

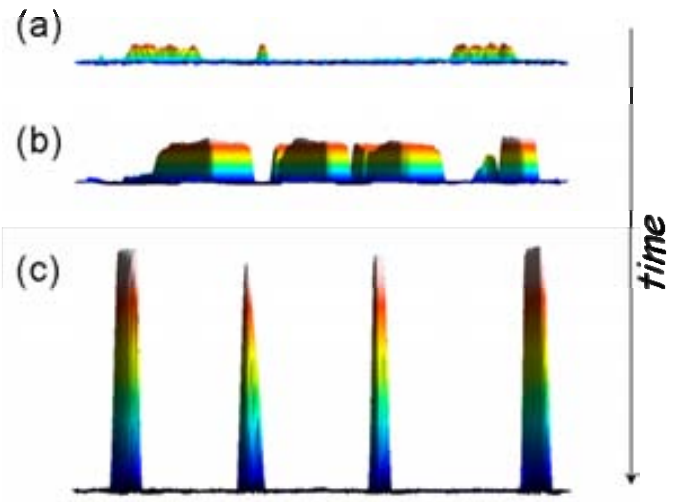

Fig. 4-29: 3D profiles of La_2O_3 nanostructures on LAO single-crystals after 30 min (a), 1 h (b) and 3 h 30 min (c) of heat treatment at 850ºC in oxidizing atmosphere. The same proportional relation between 3D profile height and real height of nanostructures has been applied to the different evolution stages. All profiles correspond to the same sample, but not to the same islands.

4.5 Summary and conclusions

In the present chapter, we have taken advantage of self-assembling and self-organizing processes for the preparation of templates with interfacial oxide nanostructures through the deposition of ultradiluted chemical solutions. The first goal has been to prove that islands' formation is spontaneously promoted in CSD-derived heteroepitaxial growth as a mechanism leading to the minimization of the total energy of the system. This tendency has been initially investigated in BZO/STO and CeO_2/LAO systems. Systematic studies based on the modification of precursor solution concentration and growth conditions (atmosphere, temperature and time) have showed the possibility to adjust the shape, size, density and distribution of the resulting interfacial nanostructures.

The study of the growth of interfacial BZO nanostructures has pointed out the important influence that growth temperature exerts on the atomic mobility of the system, leading to the formation of larger islands as higher is the annealing temperature. In BZO/STO system, enhanced atomic diffusion has also been achieved for heat treatments carried out in oxidizing atmosphere. In general, the mobility of this system has found to be quite slow since no major changes are appreciated in oxydizing atmosphere for annealings ranging from 4 to 50 hours. The optimization of precursor's solution concentration (i.e. the amount of deposited material) has become crucial to generate templates with high density of self-assembled oxide nanodots. Whereas BZO-precursor solutions of ~10^{-2} M leads to nanostructured templates with bimodal size distribution of BZO nanoislands with irregular polyhedral shapes, concentrations of ~10^{-3} M have allowed us to grow uniform 3D islands in a Volmer-Weber-like configuration. From AFM images, it has been determined that these monomodal BZO nanodots have mean lateral size of ~40 nm and mean height of ~7 nm, and a density of ~60 nanodots/μm^2. TEM images have revealed that (001)BZO nanodots grow cube-on-cube on (001)STO substrates and that they are mainly facetted with {100}-planes. Moreover, in BZO/STO system it has been observed that BZO nanodots are mostly localized at lattice steps' edges, indicative that steps act as preferential nucleation centres where the energy of the nanodot can be minimized.

In CeO_2/LAO system it has also been required to go down to concentrations of ~10^{-3} M in order to obtain templates with 3D nanoislands in Volmer-Weber-like configuration. In this case, very distinct atomic mobility has been observed depending on the oxygen pressure in heat treatment. The distinct sizes and densities of the resulting CGO nanostructures evidenced the different atomic mobility. Ar-H_2 atmosphere leads to the formation of highly in-plane anisotropic nanostructures with fairly constant short axes <50 nm and long axes ranging from 100 to 700 nm. Contrary, nanoislands processed in O_2 remained isomorphic with average lateral size of ~45 nm even for heat treatments ~6 times larger. All these dimensions were determined within AFM resolution limits. Anisotropic nanostructures exhibit low density of 10-15 wires/μm^2, whereas isomorphic ones ~ 50 dots/μm^2; as it is expected from different island's volumes and same amount of deposited material. The height of both types of CeO_2 nanostructures is ~7-10 nm. The formation of high number of vacancies in the CeO_2-fluorite structure due to the reduction of Ce^{4+} to Ce^{3+} in reducing atmosphere has been initially proposed as the mechanism leading to enhanced atomic mobility in samples processed in Ar-H_2.

Pushed by this behaviour, we looked for a strategy to always ensure the maximum concentration of oxygen vacancies in CeO_2-structure. Accordingly, CeO_2 fluorite structure was doped with Gd^{3+}. The general trend and differences observed in CeO_2 nanostructures as function of the processing atmosphere also applies to $Ce_{0.9}Gd_{0.1}O_{2-y}$ (CGO) system: isomorphic *vs.* anisotropic nanostructures, maximum lateral sizes of tens *vs.* hundreds of nanometres, slow

vs. ultrafast kinetic and coarsening mechanisms, high *vs.* low density of nanoislands, island's ordered into rows *vs.* islands' aligned along substrate's soft axes [100] and [010], etc. However, studies of growth conditions have pointed out that the formation of these elongated nanostructures, which we have referred as to *nanowires*, just occurs in a limited window of growth conditions, high temperature and low oxygen pressure. Despite oxygen vacancies seem to play an important role, they might not be the only driving force leading to such extraordinary differences. Particularly, XRD analyses of CSD-grown CGO thin films on LAO substrates have already pointed to some structural peculiarities of the system related to the nucleation of different crystallographic orientations.

Because of all that, CGO arises as a highly interesting and appealing system to investigate the thermodynamic and kinetic properties of chemically-derived strain-induced oxide nanostructures. Accordingly, next chapters 5 and 6 are entirely devoted to CGO/LAO system. The former pays special attention to the structural characterization of both kinds of CGO nanostructures and specific experiments are carried out to study in detail the kinetic and evolution processes of these nanostructures. The latter focuses on thermodynamic arguments to explain the observed shapes and behaviours, and on the analysis of the kinetic processes occurring.

Finally, in this chapter we have explored the capabilities and general validity of CSD in another set of dissimilar crystallographic structures, La_2O_3/LAO. In this case, we directly focused on the range of concentrations previously determined as most favourable for the growth of 3D interfacial nanostructures. Two sorts of islands are distinguished: large area rectangular islands with flat top which show the monoclinic phase LaOOH derived from the cubic La_2O_3, and dome-shaped larger nanoislands which crystallize in a mixture of hexagonal La_2O_3 and $La_2O_2CO_3$. A pronounced evolution of height-to-diameter has been observed in La-based nanoislands as function of the growth temperature for the same annealing period. Mean heights of ~46 nm are achieved in just 30 min of heat treatment at 1000^{o}C. At lower temperatures (i.e. 800-900^{o}C), coarsening processes also end up with La_2O_3-nanostructures of similar height after longer annealings. It must be noticed that these heights are ~6 times larger than those typically obtained for BZO and CGO nanodots under the same conditions

Hence, in the present chapter we have demonstrated the validity and generality of the combined performance of CSD and self-assembling and self-organized principles to prepare templates with well-defined and uniform oxide nanostructures. A range of optimum precursor solution concentration for the generation of interfacial nanoislands has been established. It has also been showed that temperature enhances atomic mobility in all investigated systems, whereas the role of oxygen pressure in diffusivity is specific for each phase. Hence, the

morphology and size of interfacial nanoislands strongly depends on growth conditions. However, the basic treats of the nanostructures are determined by the specific heteroepitaxial system. Particularly, surface energies and elastic relaxation energies seem to be the main clue. Besides the comprehension of the mechanisms leading to the formation of self-organized nanostructures is nowadays a great challenge, the interest in this attractive and broad fabrication route is not merely scientific. It offers a great potential for the implementation of new devices of nanometric size in fields such as ferroelectricity, piezoelectricitity, solar cells or superconductivity, specially when the nanostructuration of large areas and low cost are essential. Particularly, in chapter 7 we will show a potential application of chemically-derived nanostructured templates in the nanostructuration of high temperature superconductors.